Disease Models & Mechanisms 5, 881-894 (2012) doi:10.1242/dmm.009779

Zebrafish neurofibromatosis type 1 genes have redundant functions in tumorigenesis and embryonic development

Jimann Shin[1,*,‡], Arun Padmanabhan[2,‡], Eric D. de Groh[2,‡], Jeong-Soo Lee[1,§], Sam Haidar[3], Suzanne Dahlberg[1], Feng Guo[1], Shuning He[1], Marc A. Wolman[2], Michael Granato[2], Nathan D. Lawson[4], Scot A. Wolfe[4], Seok-Hyung Kim[5], Lilianna Solnica-Krezel[6], John P. Kanki[1], Keith L. Ligon[3], Jonathan A. Epstein[2,¶] and A. Thomas Look[1,¶]

SUMMARY

Neurofibromatosis type 1 (NF1) is a common, dominantly inherited genetic disorder that results from mutations in the *neurofibromin 1* (*NF1*) gene. Affected individuals demonstrate abnormalities in neural-crest-derived tissues that include hyperpigmented skin lesions and benign peripheral nerve sheath tumors. NF1 patients also have a predisposition to malignancies including juvenile myelomonocytic leukemia (JMML), optic glioma, glioblastoma, schwannoma and malignant peripheral nerve sheath tumors (MPNSTs). In an effort to better define the molecular and cellular determinants of NF1 disease pathogenesis in vivo, we employed targeted mutagenesis strategies to generate zebrafish harboring stable germline mutations in *nf1a* and *nf1b*, orthologues of *NF1*. Animals homozygous for loss-of-function alleles of *nf1a* or *nf1b* alone are phenotypically normal and viable. Homozygous loss of both alleles in combination generates larval phenotypes that resemble aspects of the human disease and results in larval lethality between 7 and 10 days post fertilization. *nf1*-null larvae demonstrate significant central and peripheral nervous system defects. These include aberrant proliferation and differentiation of oligodendrocyte progenitor cells (OPCs), dysmorphic myelin sheaths and hyperplasia of Schwann cells. Loss of *nf1* contributes to tumorigenesis as demonstrated by an accelerated onset and increased penetrance of high-grade gliomas and MPNSTs in adult $nf1a^{+/-}$; $nf1b^{-/-}$; $p53^{e7/e7}$ animals. *nf1*-null larvae also demonstrate significant motor and learning defects. Importantly, we identify and quantitatively analyze a novel melanophore phenotype in *nf1*-null larvae, providing the first animal model of the pathognomonic pigmentation lesions of NF1. Together, these findings support a role for *nf1a* and *nf1b* as potent tumor suppressor genes that also function in the development of both central and peripheral glial cells as well as melanophores in zebrafish.

INTRODUCTION

Type 1 neurofibromatosis (NF1) is an autosomal dominant inherited genetic disorder characterized by pigmented birthmarks known as café-au-lait spots, cutaneous and plexiform neurofibromas arising in the glial cells of the peripheral nervous system (PNS), optic pathway gliomas, cardiovascular abnormalities and learning defects (Williams et al., 2009). The disease results from mutations in the *NF1* gene, encoding the large protein neurofibromin, which contains a GTPase-activating protein-related domain (GRD) capable of inactivating the *RAS* proto-oncogene (Cawthon et al., 1990; Viskochil et al., 1990; Wallace et al., 1990). Thus, *NF1* loss results in aberrant activation of Ras signaling, which may predispose NF1 patients to a variety of cancers (Cichowski and Jacks, 2001). Heterozygous *Nf1* mutant mice develop pheochromocytoma and myeloid leukemia, whereas the conditional loss of *Nf1* in a *p53*-deficient background results in highly penetrant malignant astrocytoma formation (Jacks et al., 1994; Zhu et al., 2005a; Powers et al., 2007). Furthermore, two recent reports have identified *NF1* mutations in approximately 15-23% of human glioblastoma patients (Parsons et al., 2008; The Cancer Genome Atlas Research Network, 2008). Although these studies demonstrate a strong link between *NF1* function and high-grade glioma, the crucial signaling pathways governing the development of tumorigenesis remain to be elucidated. An animal model facilitating the rapid interrogation of epistatic and functional relationships within signaling pathways would serve as a valuable tool for probing the pathology underlying NF1-induced cell transformation.

We recently developed a zebrafish model of *NF1* deficiency using antisense morpholino oligonucleotides to produce transient gene knockdown (Padmanabhan et al., 2009; Lee et al., 2010). Two

[1]Department of Pediatric Oncology, Dana-Farber Cancer Institute, and Children's Hospital Boston, Harvard Medical School, Boston, MA 02115, USA
[2]Department of Cell and Developmental Biology, Penn Cardiovascular Institute, and the Institute for Regenerative Medicine, Perelman School of Medicine at the University of Pennsylvania, Philadelphia, PA 19104, USA
[3]Department of Medical Oncology, Center for Molecular Oncologic Pathology, Dana-Farber Cancer Institute, Harvard Medical School, Boston, MA 02215, USA
[4]Program in Gene Function and Expression, University of Massachusetts Medical School, Worcester, MA 06105, USA
[5]Department of Neurology, Vanderbilt University School of Medicine, Nashville, TN 37232, USA
[6]Department of Developmental Biology, Washington University School of Medicine in St Louis, St Louis, MO 63110, USA
*Present address: Department of Developmental Biology, Washington University School of Medicine in St Louis, St Louis, MO 63110, USA
‡These authors contributed equally to this work
§Present address: Aging Research Center, Korea Research Institute of Bioscience and Biotechnology, Daejeon 305-806, Korea
¶Authors for correspondence (epsteinj@mail.med.upenn.edu; thomas_look@dfci.harvard.edu)

Received 2 March 2012; Accepted 14 May 2012

zebrafish orthologues were identified that are highly homologous to human *NF1* at the amino acid level, sharing approximately 84% identity, including 91-93% identity within the GRD. Both genes maintain syntenic relationships with human *NF1* on chromosome 17q11.2 and are probably the result of the well-described genomic duplication event that occurred early in the evolution of teleosts (Amores et al., 1998). In our previous work with *nf1* morphants, we observed defects in both cardiovascular and nervous system development. However, due to the transient nature of morpholino gene knockdown, the analysis of *nf1*-deficient phenotypes beyond the first 3 days of life was not possible.

We report here the generation of stable mutant *nf1* zebrafish lines, using both zinc finger nuclease (ZFN) and targeting induced local lesions in genomes (TILLING) strategies, and the detailed phenotypic analysis of this new animal model of human NF1. We have successfully generated several independent null alleles of *nf1a* and *nf1b*. Mutant larvae carrying at least one wild-type *nf1a* or *nf1b* allele are viable, fertile and show no obvious phenotypes during early development. By contrast, $nf1a^{-/-}; nf1b^{-/-}$ larvae exhibit overt pigmentation defects as early as 6 days post fertilization (dpf) and do not survive beyond 10 dpf. Beginning at 4 dpf, $nf1a^{-/-}; nf1b^{-/-}$ larvae exhibit hyperplasia of oligodendrocyte progenitor cells (OPCs) and Schwann cells, as well as melanophore hypoplasia. Defects resulting from the loss of *nf1* in pigment cell and glial cell lineages mirror those often observed in the tissues of NF1 patients. In a *p53* mutant background ($p53^{e7/e7}$), $nf1a^{+/-}; nf1b^{-/-}$ fish develop high-grade gliomas and malignant peripheral nerve sheath tumors (MPNSTs), demonstrating a tumor-suppressor function for the zebrafish *nf1* orthologues. Therefore, we have developed and characterized a heritable zebrafish model of NF1 that exhibits clinical hallmarks of the disorder, including nervous system defects and increased susceptibility to tumorigenesis. Furthermore, *nf1* mutant zebrafish represent the first vertebrate model of the pathognomonic pigmentation lesions associated with NF1.

RESULTS

Generation of zebrafish *nf1a* and *nf1b* mutants

We previously identified two zebrafish orthologues of human *NF1*, *nf1a* and *nf1b*, and described the phenotypes that result from their loss of function during early development induced by antisense morpholino oligonucleotides (Padmanabhan et al., 2009; Lee et al., 2010). Although this technology readily permits transient knockdown of gene expression, its efficacy is limited to only the first few days of life. In an effort to gain a better understanding of the roles of *nf1a* and *nf1b* during development, as well as in cancer predisposition, we employed multiple approaches to develop stable lines of zebrafish harboring germline mutations in each of these genes. Using a modular approach (Zhu et al., 2011), zinc finger nucleases (ZFNs) were engineered with binding specificities directed to exon 26 of *nf1a* and exon 17 of *nf1b* (Fig. 1A,B). Paired *ZFN* mRNAs were injected into zebrafish embryos and independent target-specific mutant alleles for *nf1a* ($nf1a^{\Delta 5}$ and $nf1a^{\Delta 8}$) and *nf1b* ($nf1b^{+10}$ and $nf1b^{\Delta 55}$) were identified in the F1 generation (Fig. 1C; supplementary material Fig. S1A-D). Each of these mutations included a deletion and/or insertion within a coding exon that resulted in a frameshift, introducing premature stop codons that would be expected to truncate the neurofibromin protein upstream of the GRD (Fig. 1D,E). In a separate effort, we screened a library of *N*-ethyl-*N*-nitrosourea (ENU)-mutagenized zebrafish by targeting induced local lesions in genomes (TILLING) (Wienholds et al., 2002) and identified a single founder harboring a nonsense mutation in exon 29 of *nf1a* ($nf1a^{L1247X}$) (Fig. 1C; supplementary material Fig. S1E-G). To confirm that the targeted alleles disrupted production of full-length protein, we performed western blots using an antibody that should recognize both *nf1a* and *nf1b* with extracts prepared from 3 dpf wild-type, $nf1a^{\Delta 5/\Delta 5}; nf1b^{+/+}$, $nf1a^{+/+}; nf1b^{+10/+10}$ and $nf1a^{\Delta 5/\Delta 5}; nf1b^{+10/+10}$ larvae (Fig. 1F). We observed a complete loss of Nf1 signal in the double-homozygous null extracts. We detected only low levels of protein expression in $nf1a^{\Delta 5/\Delta 5}; nf1b^{+/+}$ mutant extracts as compared with wild-type or $nf1a^{+/+}; nf1b^{+10/+10}$ mutant extracts, which might reflect differences in expression levels of the two orthologues at 3 dpf. However, we cannot rule out the possibility that the neurofibromin antibody we used recognizes the two proteins with different affinities. We generated separate zebrafish lines with distinct null alleles of both *nf1a* and *nf1b* to provide evidence that the observed phenotypes were in fact due to *nf1* loss and did not involve any spurious passenger mutations specific to the isolation of any individual *nf1* mutant line (supplementary material Fig. S2). Because our data indicate that these various null alleles are equivalent, we refer to them without individual allelic designations henceforth ($nf1a^{-/-}$ and $nf1b^{-/-}$).

Mutants carrying at least one wild-type allele of either *nf1a* or *nf1b* are viable and fertile. However, when crossing parental genotypes that would be expected to yield $nf1a^{-/-}; nf1b^{-/-}$ progeny, none were observed in the adult population. To investigate this further, we performed quantitative survival studies. At 7 dpf, $nf1a^{-/-}; nf1b^{-/-}$ larvae began to die, with none surviving beyond 10 dpf, although 100% of wild-type larvae survived to 10 dpf (Fig. 1G). Furthermore, 100% survival at 10 dpf was also observed in $nf1a^{-/-}; nf1b^{+/+}$ (n=26), $nf1a^{+/+}; nf1b^{-/-}$ (n=22), $nf1a^{-/-}; nf1b^{+/-}$ (n=28) and $nf1a^{+/-}; nf1b^{-/-}$ (n=24) larvae. The swim bladders of $nf1a^{-/-}; nf1b^{-/-}$ larvae were frequently observed to be underinflated. However, $nf1a^{-/-}; nf1b^{-/-}$ larvae maintained the ability to both consume and transit live paramecia, suggesting that premature death was not the result of starvation (supplementary material Fig. S3). Additionally, an incompletely penetrant valvular insufficiency phenotype was appreciated in $nf1a^{-/-}; nf1b^{-/-}$ larvae, as well as in those harboring only a single wild-type *nf1* allele ($nf1a^{+/-}; nf1b^{-/-}$ and $nf1a^{-/-}; nf1b^{+/-}$) (supplementary material Movies 1-3).

OPC and Schwann cell hyperplasia in $nf1a^{-/-}; nf1b^{-/-}$ larvae

We previously described OPC hyperplasia after *nf1a* and *nf1b* morpholino knockdown in the context of a homozygous *p53* mutant background (Lee et al., 2010). To examine *nf1a* and *nf1b* function in OPCs and other tissues beyond the first few days of life, we crossed several cell-type-specific zebrafish reporter lines into *nf1a/nf1b* mutant backgrounds. At 2 dpf, *olig2* expression appeared normal in Tg(*olig2:GFP*); $nf1a^{-/-}; nf1b^{-/-}$ embryos, as assessed by both whole-mount in situ hybridization analysis of endogenous *olig2* mRNA expression and GFP expression (supplementary material Fig. S4A-D). We also evaluated *nf1* loss in Tg(*sox10:GFP*) embryos. This transgene drives GFP expression in specified ventral spinal cord OPCs, but not the neighboring motoneurons that arise from a common progenitor cell, as well as in Schwann cells of the posterior lateral line nerve (PLLn). At 2 dpf, similar numbers of *sox10*:GFP-positive OPCs were detected

in the dorsal and ventral spinal cord of wild-type and *nf1a*$^{-/-}$; *nf1b*$^{-/-}$ embryos (supplementary material Fig. S4E,F). Examination of *nf1*-null PNS Schwann cells at 2 dpf showed no effect on the number of *sox10*:GFP-expressing cells associated with the PLLn, which innervate skin mechanosensory neuromast cells (supplementary material Fig. S4G,H).

However, *nf1a*$^{-/-}$; *nf1b*$^{-/-}$ larvae exhibited increased numbers of OPCs at 4 dpf compared with controls, as evidenced by an excess

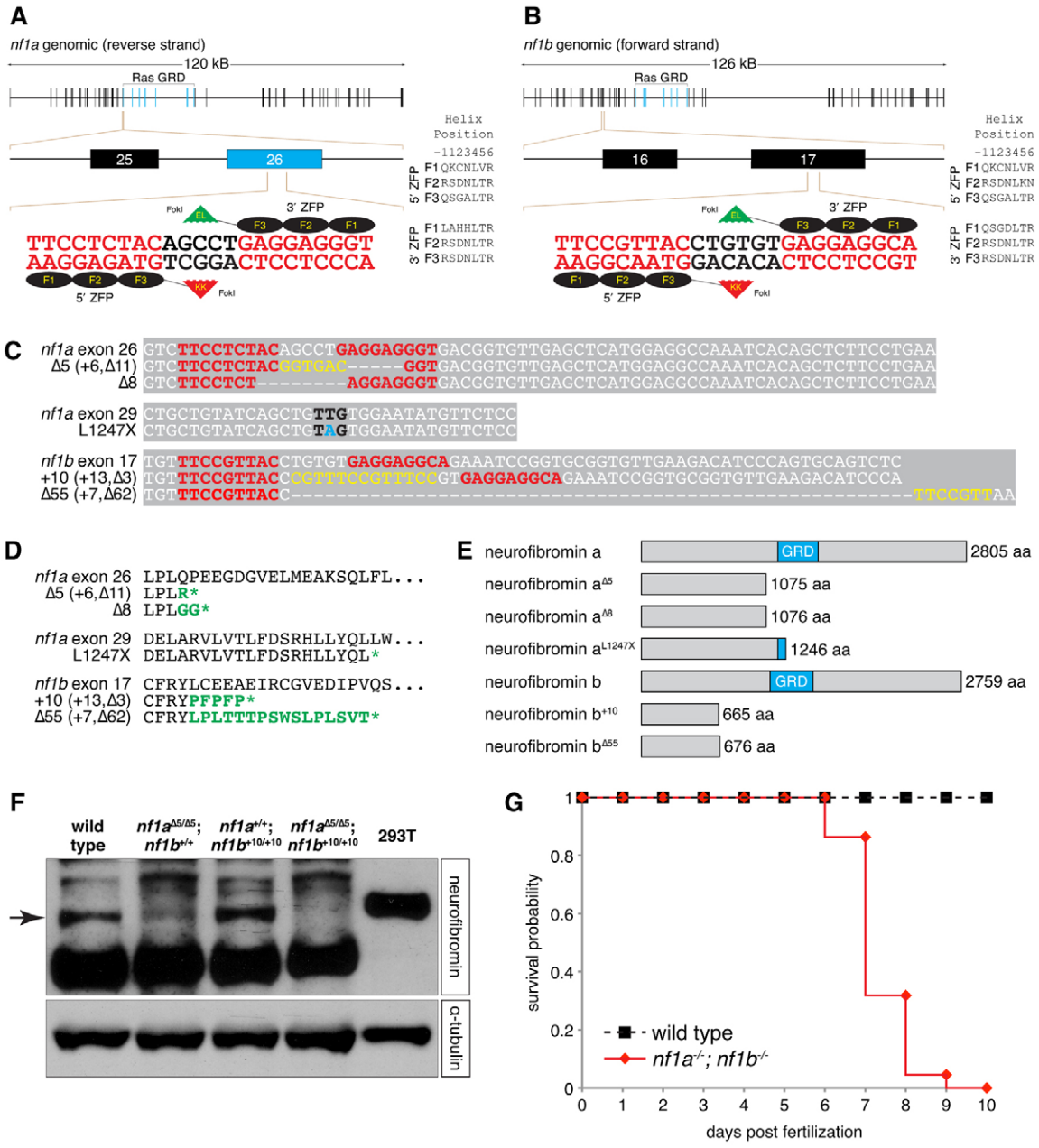

Fig. 1. ZFN and TILLING strategies generate null alleles of zebrafish *nf1a* and *nf1b*. (A,B) Scheme of site targeted for ZFN-mediated cleavage in exon 26 of *nf1a* and exon 17 of *nf1b*. (C) Alignments of nucleotide sequences from wild-type and mutant *nf1a* and *nf1b* alleles. ZFN target sites appear in red. Yellow bases represent insertions that arise from repair of ZFN-induced mutagenic lesions. Black bases correspond to the mutated codon in the *nf1a*^{L1247X} allele generated by a TILLING strategy, with the mutated base appearing in blue. (D) ZFN-induced mutagenic lesions in *nf1a* and *nf1b* produce frameshift mutations that lead to truncated protein products following short regions of altered translation, which are indicated in green. The nonsense mutation in the *nf1a*^{L1247X} allele generated by a TILLING strategy also appears in green. (E) The truncated protein products predicted by the ZFN- and TILLING-induced mutant *nf1a/nf1b* alleles all harbor complete or partial loss of the neurofibromin GAP-related domain (GRD). (F) Western blot analysis for neurofibromin in protein lysates from 3 dpf wild-type, *nf1a*$^{Δ5/Δ5}$; *nf1b*$^{+/+}$, *nf1a*$^{+/+}$; *nf1b*$^{+10/+10}$ and *nf1a*$^{Δ5/Δ5}$; *nf1b*$^{+10/+10}$ zebrafish larvae (100 μg each) or 293T cells (25 μg) demonstrates absence of Nf1 protein in *nf1a*$^{-/-}$; *nf1b*$^{-/-}$ larvae. Equal loading was confirmed by stripping the membrane and reprobing for α-tubulin. (G) Kaplan-Meier survival analysis demonstrates that 100% of *nf1a*$^{-/-}$; *nf1b*$^{-/-}$ larvae (*n*=22) die by 10 dpf as compared with 0% of wild-type larvae (*n*=27).

of dorsally migrated *olig2*:GFP-positive OPCs (Fig. 2A,B) along with increased numbers of both dorsally and ventrally positioned *sox10*:GFP-positive OPCs (Fig. 2C,D), consistent with our analyses of *nf1* morphants at 3 dpf (Lee et al., 2010). In addition, we observed an increase in *sox10*:GFP-positive Schwann cells associated with the PLLn (Fig. 2E,F). This increase in PLLn Schwann cell number was not associated with altered proliferation of these cells (supplementary material Fig. S5A-F). To assess the roles of *nf1a* and *nf1b* in the developing radial glial cells of the spinal cord, *nf1a/nf1b* mutants were crossed into the Tg(*gfap:GFP*) line, which expresses GFP from the glial fibrillary acidic protein (*gfap*) promoter. At 4 dpf, *nf1a*$^{-/-}$; *nf1b*$^{-/-}$ larvae harboring a *gfap:GFP* transgene demonstrated no readily discernible differences in *gfap*:GFP-positive spinal cord radial glial cells as compared with wild-type larvae (supplementary material Fig. S4I,J). However, *gfap* expression in the extensive processes of radial glial cells precludes precise quantification and might obscure subtle differences.

To determine whether neuronal numbers increased in concert with OPCs in *nf1a/nf1b* mutant larvae, we used anti-HuC/D and anti-SOX10 antibodies (see Methods) to discriminate between *olig2*:GFP-positive neurons and OPCs, respectively. No difference between the number of *olig2*:GFP-positive and HuC/D-positive neurons was appreciable in 4 dpf spinal cord sections from wild-type and *nf1a*$^{-/-}$; *nf1b*$^{-/-}$ larvae (Fig. 2G,H, green and magenta; Fig. 2K). However, the numbers of *olig2*:GFP-positive and Sox10-positive OPCs (Fig. 2G,H, arrowheads; Fig. 2L) and PLLn Schwann cells (Fig. 2I,J,M) were significantly increased at 4 dpf in *nf1a*$^{-/-}$; *nf1b*$^{-/-}$ larvae relative to wild-type controls. OPC cell numbers continued to increase in *nf1a*$^{-/-}$; *nf1b*$^{-/-}$ larvae at 8 dpf, as reflected by increased numbers of dorsally localizing *olig2*:GFP-positive OPCs as well as both dorsally and ventrally localizing *sox10*:GFP-positive OPCs (supplementary material Fig. S4M-P). Increased numbers of *sox10*:GFP-expressing PLLn Schwann cells were also evident in *nf1a*$^{-/-}$; *nf1b*$^{-/-}$ larvae at 8 dpf (supplementary material Fig. S4Q,R). Thus, loss of *nf1a* and *nf1b* does not affect the specification of OPCs at 2 dpf, but instead promotes the progressive expansion of OPCs without a concomitant increase in neuronal cell numbers. Furthermore, *nf1a/nf1b* loss triggers Schwann cell hyperplasia beginning at 4 dpf.

Immunohistochemical analysis using the Zrf1 antibody, which labels Gfap in zebrafish, showed coexpression with GFP expressed from the *gfap:GFP* transgene and revealed a similar pattern of expression in wild-type and *nf1a*$^{-/-}$; *nf1b*$^{-/-}$ larvae at 4 dpf (supplementary material Fig. S6A,B). Zebrafish radial glial cells also express brain lipid-binding protein (Blbp), and immunohistochemical analysis of wild-type and *nf1a*$^{-/-}$; *nf1b*$^{-/-}$ spinal cords with an anti-BLBP antibody at 4 dpf revealed an obvious decrease in Blbp expression in the *gfap*:GFP-positive radial glia of *nf1a*$^{-/-}$; *nf1b*$^{-/-}$ larvae (supplementary material Fig. S6C,D). These results suggest that although *gfap*:GFP-positive radial glial cells in *nf1a*$^{-/-}$; *nf1b*$^{-/-}$ larvae appear normal in number, they fail to express appropriate levels of Blbp indicating a defect in gliogenesis. An additional abnormality of gliogenesis was observed at 8 dpf as a disruption in the regular segmental pattern of glial process outgrowth in Tg(*gfap:GFP*); *nf1a*$^{-/-}$; *nf1b*$^{-/-}$ larvae (supplementary material Fig. S4K,L).

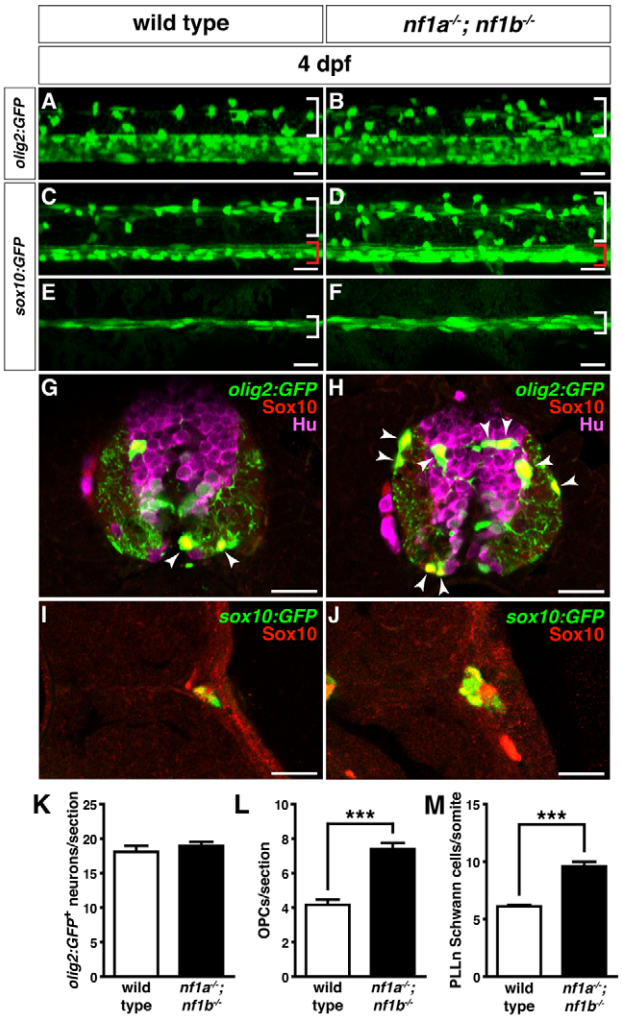

Fig. 2. Loss of *nf1a* and *nf1b* causes hyperplasia of OPCs and Schwann cells. (A,B) Confocal images of spinal cords in *nf1a*$^{-/-}$; *nf1b*$^{-/-}$; Tg(*olig2:GFP*) larvae (B) demonstrate increased numbers of dorsally migrating (white brackets) *olig2*:GFP-positive OPCs as compared with wild-type; Tg(*olig2:GFP*) larvae (A) at 4 dpf. (C,D) Confocal images of spinal cord in *nf1a*$^{-/-}$; *nf1b*$^{-/-}$; Tg(*sox10:GFP*) larvae (D) demonstrate increased numbers of both dorsally (white brackets) and ventrally (red brackets) positioned *sox10*:GFP-positive OPCs as compared with wild-type; Tg(*sox10:GFP*) larvae (C) at 4 dpf. (E,F) *nf1a*$^{-/-}$; *nf1b*$^{-/-}$; Tg(*sox10:GFP*) larvae (F) show an increased number of *sox10*:GFP-positive Schwann cells associated with the peripheral lateral line nerve (PLLn; white brackets) as compared with wild-type; Tg(*sox10:GFP*) larvae (E) at 4 dpf. (G,H) Neuronal numbers (*olig2*:GFP- [green], HuC/D- [magenta] positive) do not increase in concert with OPCs (*olig2*:GF- [green], Sox10- [red] positive; arrowheads) in transverse sections through the spinal cord of *nf1a*$^{-/-}$; *nf1b*$^{-/-}$; Tg(*olig2:GFP*) larvae (H) as compared to wild-type; Tg(*olig2:GFP*) larvae (G) at 4 dpf. (I,J) Increased numbers of PLLn Schwann cells (*sox10*:GFP- [green], Sox10- [red] positive) are appreciated in transverse sections of *nf1a*$^{-/-}$; *nf1b*$^{-/-}$; Tg(*sox10:GFP*) larvae (J) as compared with wild-type; Tg(*sox10:GFP*) (I) larvae at 4 dpf. (K,L) Quantification of neurons (*olig2*:GFP-, HuC/D-positive cells) (K) and OPCs (*olig2*:GFP-, Sox10-positive cells) (L) from transverse sections through the spinal cord of wild-type; Tg(*olig2:GFP*) and *nf1a*$^{-/-}$; *nf1b*$^{-/-}$; Tg(*olig2:GFP*) larvae at 4 dpf. Values indicate mean + s.e.m. per section (n=30 from five each of wild-type and *nf1a*$^{-/-}$; *nf1b*$^{-/-}$ larvae). (M) Quantification of *sox10*:GFP-positive Schwann cells in the PLLn of wild-type; Tg(*sox10:GFP*) and *nf1a*$^{-/-}$; *nf1b*$^{-/-}$; Tg(*sox10:GFP*) larvae at 4 dpf. Values indicate mean + s.e.m. per hemisegment (n=5 each for wild-type and *nf1a*$^{-/-}$; *nf1b*$^{-/-}$ larvae). ***P<0.001. Scale bars: 20 µm.

OPC hyperplasia in *nf1a*$^{-/-}$; *nf1b*$^{-/-}$ larvae results from increased proliferation

In *nf1a*$^{-/-}$; *nf1b*$^{-/-}$ larvae, OPC numbers were increased relative to control animals at 4 dpf, but not at 2 dpf, suggesting that *nf1*-null OPCs might proliferate faster during this time period. We assessed OPC proliferation by labeling larvae with BrdU for 12 hours starting at 3.5, 4.5 and 5.5 dpf followed by immunohistochemical analysis of transverse sections through the spinal cord. By 4 dpf and continuing through 6 dpf, the number of *olig2*:GFP-positive and Sox10-positive OPCs in *nf1*-null larvae was significantly increased in comparison with wild-type controls (Fig. 3A-H, arrows; Fig. 3I). Mutant larvae further exhibited significantly increased numbers of *olig2*:GFP-, Sox10- and BrdU-positive OPCs at 4 and 5 dpf as compared with controls, indicating that neurofibromin normally suppresses the proliferation of OPCs during this period of development (Fig. 3A-H, arrowheads; Fig. 3J). There was little detectable BrdU incorporation at 6 dpf in either mutant or control populations.

Myelination is aberrant in *nf1a*$^{-/-}$; *nf1b*$^{-/-}$ larvae

We evaluated the ability of *nf1a*$^{-/-}$; *nf1b*$^{-/-}$ OPCs to differentiate appropriately by examining the gene expression levels of proteolipid protein 1a (*plp1a*) and myelin basic protein (*mbp*), markers of differentiated oligodendrocytes, in wild-type and mutant larvae at 5 dpf. In *nf1*-null larvae, fewer *plp1a*-positive cells were detected in the midbrain and hindbrain regions (Fig. 4A,B) as well as along the dorsal and ventral spinal cords (Fig. 4C,D) as compared with controls. Central nervous system (CNS) expression of *mbp*, on the other hand, was indistinguishable between wild-type and *nf1a*$^{-/-}$; *nf1b*$^{-/-}$ larvae at 5 dpf (supplementary material Fig. S7). However, *mbp* expression was elevated in Schwann cells of the PLLn in *nf1a*$^{-/-}$; *nf1b*$^{-/-}$ larvae as compared with controls (Fig. 4E,F, arrowheads). These data are consistent with perturbed oligodendrocyte differentiation in the CNS as well as in PNS Schwann cells associated with the PLLn of *nf1a*$^{-/-}$; *nf1b*$^{-/-}$ larvae.

We went on to examine the ultrastructure of myelinated CNS axons in control and *nf1-null* larvae by transmission electron microscopy (TEM). At 8 dpf, oligodendritic myelin sheaths were tightly wrapped around CNS axons in the ventral spinal cord of wild-type larvae (Fig. 4G,I). By contrast, *nf1a*$^{-/-}$; *nf1b*$^{-/-}$ axons were loosely encircled by multiple lamellae rather than by compact myelin sheaths, indicating that neurofibromin is required for the normal formation of the concentric layers of oligodendrocyte membranes that enwrap neuronal axons of the CNS to promote neural conduction (Fig. 4H,J).

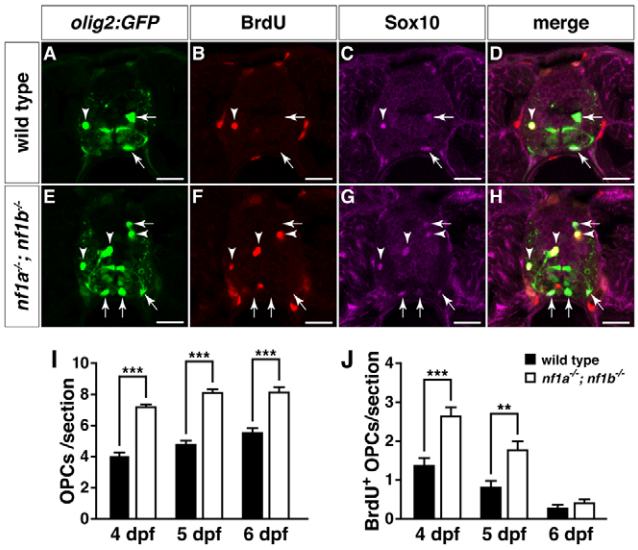

Fig. 3. Increased proliferation drives OPC hyperplasia in *nf1a*$^{-/-}$; *nf1b*$^{-/-}$ larvae. (A-H) Transverse spinal cord sections of wild-type; Tg(*olig2:GFP*) (A-D) and *nf1a*$^{-/-}$; *nf1b*$^{-/-}$; Tg(*olig2:GFP*) larvae (E-H) labeled with anti-BrdU antibody (B,F, red) or anti-SOX10 antibody (C,G, magenta) at 4 dpf. Arrows indicate BrdU-negative, Tg(*olig2:GFP*)-, Sox10-positive OPCs. Arrowheads indicate BrdU-positive, Tg(*olig2:GFP*)-, Sox10-positive OPCs. (I,J) Quantification of total (I) and BrdU-positive OPCs (J) from transverse spinal cord sections of wild-type; Tg(*olig2:GFP*) and *nf1a*$^{-/-}$; *nf1b*$^{-/-}$; Tg(*olig2:GFP*) larvae at 4, 5 and 6 dpf. Values indicate mean + s.e.m. per section (n=30 from five each of wild-type and *nf1a*$^{-/-}$; *nf1b*$^{-/-}$ larvae). **P<0.01; ***P<0.001. Scale bars: 20 µm.

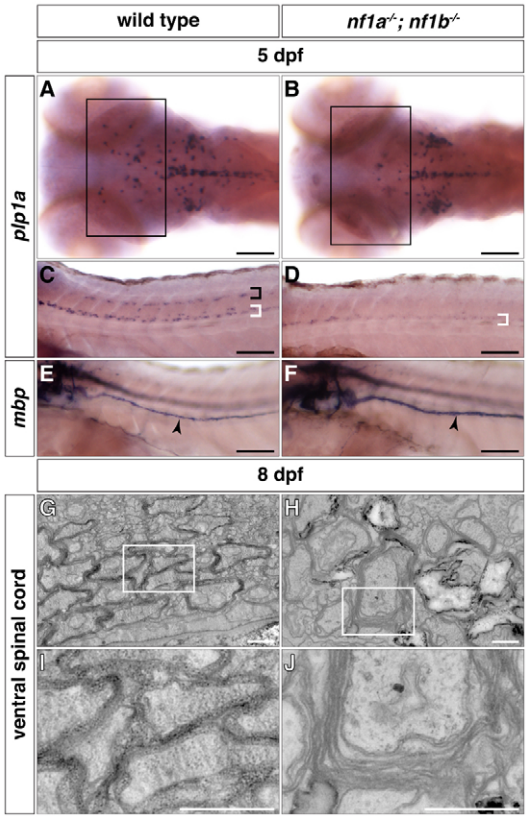

Fig. 4. *nf1a*$^{-/-}$; *nf1b*$^{-/-}$ larvae exhibit myelination defects. (A-D) *plp1a* expression is decreased in glial cells of the midbrain and hindbrain regions (A,B, boxes) as well as the dorsal (black bracket) and ventral (white brackets) spinal cord of *nf1a*$^{-/-}$; *nf1b*$^{-/-}$ larvae (B,D) as compared to wild-type larvae (A,C) by whole-mount in situ hybridization at 5 dpf. (E,F) *mbp* expression is elevated in Schwann cells of the PLLn (arrowheads) of *nf1a*$^{-/-}$; *nf1b*$^{-/-}$ larvae (F) as compared to wild-type larvae (E) by whole-mount in situ hybridization at 5 dpf. (G-J) Transverse sections through the ventral spinal cord *nf1a*$^{-/-}$; *nf1b*$^{-/-}$ larvae (H, boxed region magnified in J) demonstrate defects in formation of compact myelin sheaths as compared with wild-type larvae (G, boxed region magnified in I) at 8 dpf. Scale bars: 100 µm (A-F) and 0.5 µm (G-J).

Loss of *nf1a* and *nf1b* causes upregulation of Ras signaling in the spinal cord

Given the well-described role of neurofibromin as a negative regulator of Ras, we hypothesized that *nf1* loss in our mutants would lead to activation of downstream effector pathways. Western blot analysis of whole larvae extracts revealed an upregulation of phosphorylated ERK1 and ERK2 (pERK1/2) in *nf1a*$^{-/-}$; *nf1b*$^{-/-}$ larvae at 3 dpf, whereas levels in *nf1a*$^{-/-}$; *nf1b*$^{+/+}$ and *nf1a*$^{+/+}$; *nf1b*$^{-/-}$ larvae remained unchanged (Fig. 5A). These data are consistent with the absence of functioning neurofibromin protein in *nf1a*$^{-/-}$; *nf1b*$^{-/-}$ larvae and support functional redundancy between *nf1a* and *nf1b*. We next assessed the activation of Ras effector pathways in the spinal cords of wild-type, *nf1a*$^{+/-}$; *nf1b*$^{-/-}$, *nf1a*$^{-/-}$; *nf1b*$^{+/-}$ and *nf1a*$^{-/-}$; *nf1b*$^{-/-}$ animals by immunohistochemical analysis of transverse larval sections. Antibodies directed against HuC/D, pERK1/2, and phosphorylated S6 (pS6) were used to label neurons and assess activation of ERK and mTOR signaling pathways, respectively (Fig. 5B-Q). Although pERK1/2 staining was only minimally observed in a few neurons and portions of spinal cord white matter at 4 dpf in wild-type larvae (Fig. 5B,N), a striking upregulation of pERK1/2 was detected in *nf1a*$^{-/-}$; *nf1b*$^{-/-}$ larvae (Fig. 5E,Q). Increased ERK signaling was also noted at 3 dpf in spinal cord neurons and white matter of *nf1a*$^{-/-}$; *nf1b*$^{-/-}$ larvae, but was absent at 2 dpf (supplementary material Fig. S8). Although pS6 signaling was evident in multiple spinal cord neurons, we observed no differences in these cells between wild-type and *nf1* mutant animals at 2, 3 or 4 dpf (supplementary material Fig. S8Ae-Ah,Be-Bh; Fig. 5F-I). These data suggest that activation of mTOR signaling (as assessed by S6 phosphorylation) is not altered, at least in the spinal cord following *nf1* loss.

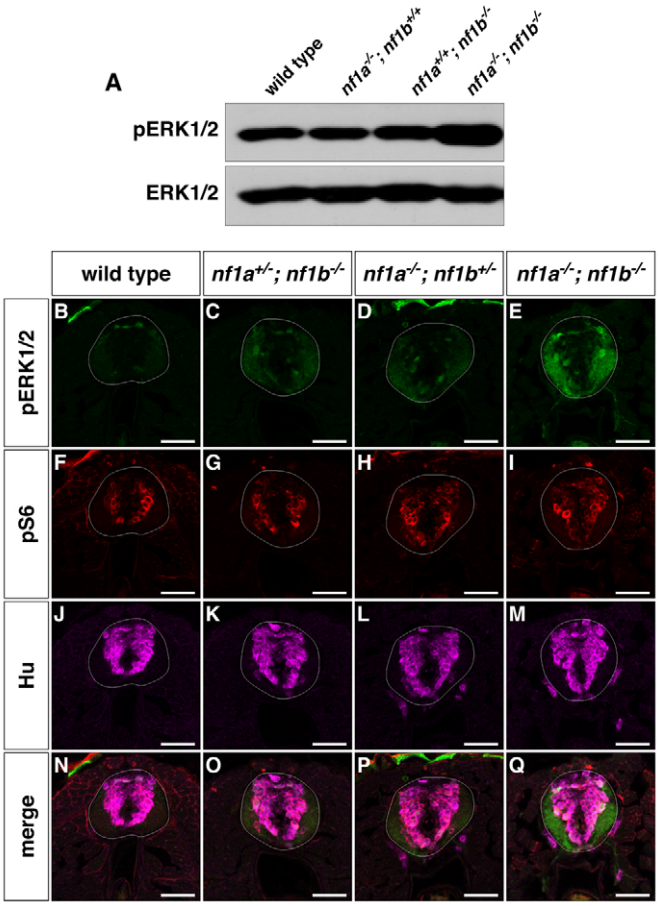

Fig. 5. *nf1a*/*nf1b* mutants exhibit upregulation of pERK1/2. (A) Western blot analysis for pERK1/2 in protein lysates prepared from wild-type, *nf1a*$^{-/-}$; *nf1b*$^{+/+}$, *nf1a*$^{+/+}$; *nf1b*$^{-/-}$ and *nf1a*$^{-/-}$; *nf1b*$^{-/-}$ larvae (100 µg) reveals increased pERK1/2 levels in *nf1a*$^{-/-}$; *nf1b*$^{-/-}$ larvae as compared with wild-type, *nf1a*$^{-/-}$; *nf1b*$^{+/+}$ and *nf1a*$^{+/+}$; *nf1b*$^{-/-}$ larvae at 3 dpf. Equal loading was confirmed by stripping the membrane and reprobing for total ERK1/2. (B-Q) Transverse spinal cord sections of wild-type (B,F,J,N), *nf1a*$^{+/-}$; *nf1b*$^{-/-}$ (C,G,K,O), *nf1a*$^{-/-}$; *nf1b*$^{+/-}$ (D,H,L,P) and *nf1a*$^{-/-}$; *nf1b*$^{-/-}$ (E,I,M,Q) larvae labeled with anti-pERK1/2 antibody (B-E, green), anti-pS6 antibody (F-I, red), or anti-HuC/D antibody (J-M, magenta) demonstrate marked upregulation of pERK1/2 in *nf1a*$^{-/-}$; *nf1b*$^{-/-}$ larvae and intermediate levels of pERK1/2 in larvae harboring a single functioning *nf1* allele as compared with wild-type larvae at 4 dpf (*n*=5 each for wild-type and mutant larvae). Scale bars: 40 µm.

nf1 and *p53* cooperate to accelerate zebrafish tumorigenesis in vivo

Mammalian *NF1* has been shown to be a potent tumor suppressor; however, we did not identify any tumors over 18 months of observation in adult zebrafish homozygous for either mutant *nf1* allele alone (*nf1a*$^{-/-}$; *nf1b*$^{+/+}$ or *nf1a*$^{+/+}$; *nf1b*$^{-/-}$) or in combination with heterozygous loss of the remaining allele (*nf1a*$^{+/-}$; *nf1b*$^{-/-}$ or *nf1a*$^{-/-}$; *nf1b*$^{+/-}$). Loss of p53 has been shown to cooperate with NF1 (Cichowski et al., 1999; Vogel et al., 1999) as well as other mutations that activate Ras signaling (Eliyahu et al., 1984; Parada et al., 1984; Kemp et al., 1994; Tanaka et al., 1994; Hundley et al., 1997) in mammalian tumorigenesis, so we next bred *p53* mutant zebrafish into an *nf1*-mutant background to generate *nf1a*$^{+/-}$; *nf1b*$^{-/-}$; *p53*$^{e7/e7}$ fish. These animals were incrossed to derive *nf1a*$^{+/+}$; *nf1b*$^{-/-}$; *p53*$^{e7/e7}$ and *nf1a*$^{+/-}$; *nf1b*$^{-/-}$; *p53*$^{e7/e7}$ fish, which were subsequently monitored carefully for tumorigenesis. At 31 weeks post fertilization (wpf), *nf1a*$^{+/-}$; *nf1b*$^{-/-}$; *p53*$^{e7/e7}$ fish began to develop tumors with high penetrance although only one *nf1a*$^{+/+}$; *nf1b*$^{-/-}$; *p53*$^{e7/e7}$ fish developed a tumor at 44 wpf (Fig. 6A). At 45 wpf, tumor penetrance was higher in *nf1a*$^{+/-}$; *nf1b*$^{-/-}$; *p53*$^{e7/e7}$ fish (24/39; 62%) than in *nf1a*$^{+/+}$; *nf1b*$^{-/-}$; *p53*$^{e7/e7}$ fish (1/14; 7%). We have previously reported that *p53*$^{e7/e7}$ fish with wild-type *nf1* alleles develop MPNSTs. These tumors did not begin to develop until 41 weeks of age, which was similar to the results with *nf1a*$^{+/+}$; *nf1b*$^{-/-}$; *p53*$^{e7/e7}$ animals (Fig. 6A). Furthermore, the penetrance of tumors in *p53*-null animals was only 28% by 66 wpf (Berghmans et al., 2005). Thus, the combined loss of *p53* and 3 of 4 *nf1* alleles in zebrafish markedly accelerates the onset and increases the penetrance of tumors as compared with the loss of *p53* alone or the concomitant loss of *p53* and both alleles of *nf1b*, but with intact *nf1a*.

Tumors in *nf1a*$^{+/-}$; *nf1b*$^{-/-}$; *p53*$^{e7/e7}$ fish were observed in the brain (*n*=2), eye (*n*=8), gill (*n*=1), abdomen (*n*=8) and trunk (*n*=5). Brain tumors developed very early (31 and 33 wpf) (Fig. 6A, arrows) and demonstrated features of diffuse high-grade gliomas, whereas all other tumor types were most consistent with MPNSTs (Fig. 6B-G). Histopathologically, the brain tumors were highly cellular and composed of ovoid to rounded cells with marked nuclear pleomorphism and diffuse single cell infiltration of parenchyma, including pre-existing neurons (Fig. 7A-F). Occasional mitoses were

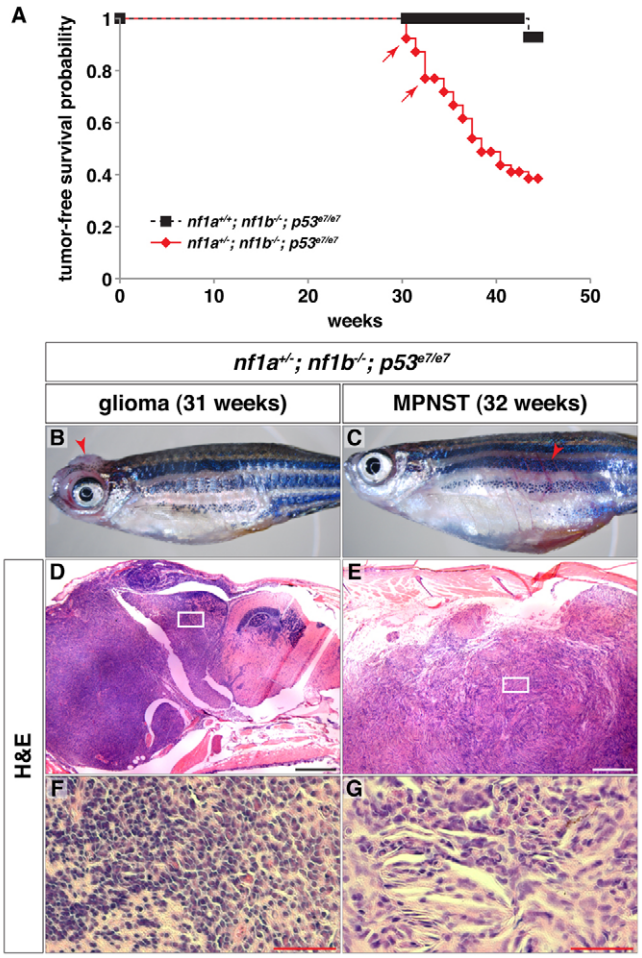

Fig. 6. *nf1a*/*nf1b* mutants demonstrate increased susceptibility to tumorigenesis in a *p53* mutant background. (A) Kaplan-Meier tumor-free survival analysis for $nf1a^{+/-}; nf1b^{-/-}; p53^{e7/e7}$ (n=39) animals demonstrates significantly decreased survival as compared with $nf1a^{+/+}; nf1b^{-/-}; p53^{e7/e7}$ (n=14) animals (P<0.001). Arrows indicate ages at which animals were identified with brain tumors demonstrating features of diffuse high-grade gliomas. (B,C) 31-week-old $nf1a^{+/-}; nf1b^{-/-}; p53^{e7/e7}$ animal with a high-grade glioma (B, arrowhead) and 32-week-old $nf1a^{+/-}; nf1b^{-/-}; p53^{e7/e7}$ animal with a malignant peripheral nerve sheath tumor (MPNST) (C, arrowhead). (D-G) H&E staining of sagittal sections through the high-grade optic glioma (D, boxed area magnified in F) or MPNST (E, boxed area magnified in G). Scale bars: 200 μm (D,E) and 50 μm (F,G).

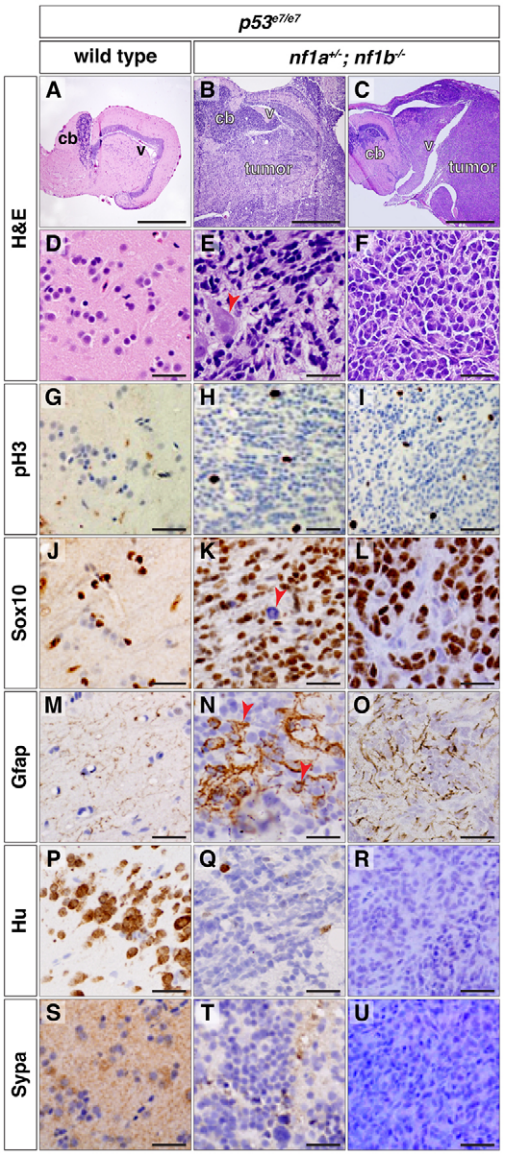

Fig. 7. Tumors from $nf1a^{+/-}; nf1b^{-/-}; p53^{e7/e7}$ animals express glial markers. (A-F) H&E staining of sagittal sections through $p53^{e7/e7}$ brain tissue (A,D) or brain tumors in $nf1a^{+/-}; nf1b^{-/-}; p53^{e7/e7}$ animals at 31 (B,E) and 33 (C,F) wpf (cb, cerebellum; v, ventricle). The arrowhead in E shows infiltration of a single cell through the parenchyma and around normal neurons.
(G-U) Immunohistochemical analyses for phosphorylated histone H3 (G-I, pH3), SRY-box 10 (J-L, Sox10), glial fibrillary acidic protein (M-O, Gfap), HuC/D (P-R, Hu) and synaptophysin (S-U, Sypa) on sagittal sections through $p53^{e7/e7}$ brain tissue (G,J,M,P,S) or brain tumors in $nf1a^{+/-}; nf1b^{-/-}; p53^{e7/e7}$ animals at 31 (H,K,N,Q,T) and 33 (I,L,O,R,U) wpf demonstrate occasional mitoses in tumor tissue (H,I) with most tumor cells staining positive for the oligodendroglial marker Sox10 (K,L), a Sox10-negative subpopulation (K, arrowhead), an astrocytic component (N, arrowheads and O) and the absence of mature neuronal markers HuC/D (Q,R) or synaptophysin (T,U). Scale bars: 450 μm (A-C) and 20 μm (D-U).

identified, but no necrosis or vascular proliferation was detected (Fig. 7G-I). Assessment of tumor lineage by immunohistochemical analysis showed that approximately 80% of tumor cells stained positive for the oligodendroglial marker Sox10, with little staining in matched wild-type tissue (Fig. 7J-L). The presence of a Sox10-negative tumor cell subpopulation is consistent with the level of heterogeneity for oligodendroglial transcription factors, such as Sox10 and Olig2, and is characteristic of astrocytic or mixed gliomas as compared with pure oligodendroglial class tumors (Fig. 7K, arrowhead) (Ligon et al., 2004; Bannykh et al., 2006). Staining for the astrocytic marker Gfap (Fig. 7M-O) highlighted a subpopulation of cells within the tumor with coarse, irregular cytoplasmic processes also consistent with the presence of an astrocytic lineage component (Fig. 7N, arrowheads). Tumor cells did not express the mature neuronal markers HuC/D or synaptophysin (Sypa), consistent with their glial origin (Fig. 7P-U).

Immunohistochemical analysis for pERK1/2 and pS6 to assess activation of ERK and mTOR signaling pathways, respectively (supplementary material Fig. S9A-F) revealed increased pERK1/2 staining in the more malignant of these two brain tumors, with normal amounts of pS6 (supplementary material Fig. S9C,D). The more hyperplastic brain tumor showed increased pERK1/2 and pS6 staining (supplementary material Fig. S9E,F). These data demonstrate that some, but not all, brain tumors in *nf1a*$^{+/-}$; *nf1b*$^{-/-}$; *p53*$^{e7/e7}$ animals demonstrate hyperactivation of ERK and mTOR pathways, consistent with mouse and human *NF1*-derived MPNSTs and gliomas (Dasgupta et al., 2005; Zhu et al., 2005b). Collectively, these findings suggest that the tumors were high-grade gliomas most closely resembling human anaplastic astrocytoma or anaplastic oligoastrocytoma WHO grade III. Furthermore, MPNSTs (Fig. 6C,E,G) exhibited spindle-shaped tumor cells and extensive necrosis consistent with this tumor type (Ducatman et al., 1986; Wanebo et al., 1993; Hirose et al., 1998). Taken together, we conclude that *nf1a* and *nf1b* mutations cooperate with *p53* loss to generate high-grade gliomas and MPNSTs.

nf1a$^{-/-}$; *nf1b*$^{-/-}$ larvae show motor and learning deficits

Deficits in motor coordination and cognition, including learning and memory, are characteristic of NF1 patients and animal models. To examine motor behavior and cognition in *nf1a*$^{-/-}$; *nf1b*$^{-/-}$ larvae, we performed kinematic analysis of the short-latency C-start (SLC), a highly stereotyped yet modifiable acoustic startle reflex in the zebrafish (Burgess and Granato, 2007a; Wolman et al., 2011). Unlike their siblings, *nf1a*$^{-/-}$; *nf1b*$^{-/-}$ larvae showed a deficit in short-term SLC habituation when presented with repetitive acoustic stimulation (supplementary material Fig. S10A). Furthermore, *nf1a*$^{-/-}$; *nf1b*$^{-/-}$ larvae performed kinematically weaker SLC responses, as indicated by decreased head turning angle, maximum angular velocity and distance traveled following delivery of an acoustic stimulus (supplementary material Fig. S10B-D). Taken together, these data support the hypothesis that *nf1a* and *nf1b* function redundantly during zebrafish development and that only one of the four wild-type *nf1* alleles is required for phenotypically normal embryonic development, motor behavior and cognition.

nf1 mutants exhibit melanophore defects

Notably, *nf1* null larvae displayed aberrant lateral stripe pigmentation as compared with wild-type controls at 6 dpf (Fig. 8A-D). This phenotype was first appreciable at 4 dpf and was manifested as a disruption in the uniform pattern of melanophores arranged along the lateral stripes (Fig. 8B,D, brackets). To further investigate this phenotype, we quantified melanophore numbers along the lateral stripes of 3 and 6 dpf wild-type and *nf1a*$^{-/-}$; *nf1b*$^{-/-}$ larvae. No significant differences in the number of melanophores comprising the 3 dpf lateral stripes were appreciable in any combination of mutant *nf1* alleles as compared with sibling wild-type controls (supplementary material Fig. S11). However, at 6 dpf, *nf1a*$^{-/-}$; *nf1b*$^{-/-}$ larvae exhibited a significant reduction in the number of lateral stripe melanophores (Fig. 8E). Less severe, but still significant, decreases were also noted in larvae carrying two or three mutant *nf1* alleles (Fig. 8E). No difference in the number of apoptotic cells between wild-type and mutant larvae was discernible at 3 dpf (68.1±11 cells/larva, *n*=12 wild-type versus

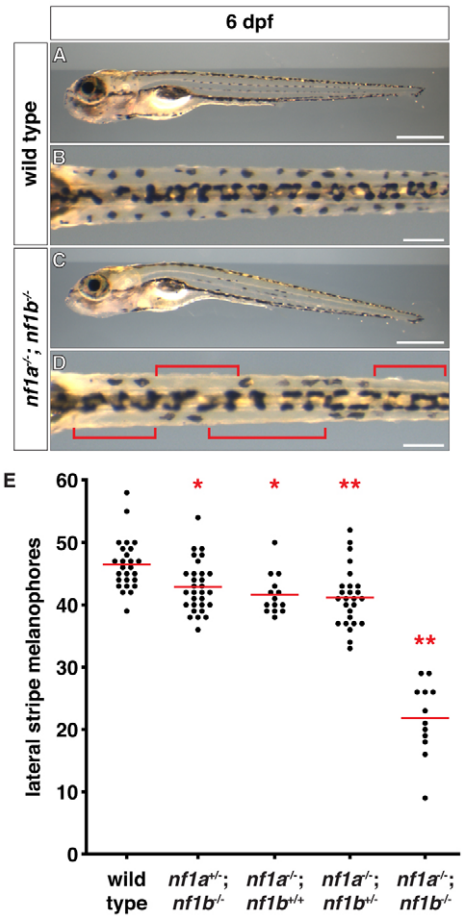

Fig. 8. *nf1* mutants display decreased lateral stripe melanophores. (A-D) Lateral stripe melanophores of wild-type (A,B) larvae demonstrate a normal uniform pattern that is absent in *nf1a*$^{-/-}$; *nf1b*$^{-/-}$ larvae (C,D) at 6 dpf. The brackets in D highlight regions where melanophores are absent. (E) Quantification of lateral stripe melanophores from wild-type (*n*=26), *nf1a*$^{+/-}$; *nf1b*$^{-/-}$ (*n*=30), *nf1a*$^{-/-}$; *nf1b*$^{+/+}$ (*n*=14), *nf1a*$^{-/-}$; *nf1b*$^{+/-}$ (*n*=26) and *nf1a*$^{-/-}$; *nf1b*$^{-/-}$ (*n*=12) larvae at 6 dpf. Each point represents the number of lateral stripe melanophores in an individual embryo and red lines indicate mean values. *P<0.05, **P<0.01. Scale bars: 0.5 mm (A,C) and 150 µm (B,D).

63.8±8.5, *n*=12 mutants; P=0.27) (supplementary material Fig. S12A-F). Serial observation of melanophore development in individual *nf1a*$^{-/-}$; *nf1b*$^{-/-}$ and wild-type larvae revealed a defect of migration or differentiation of regeneration and metamorphic lineage melanophores. At 3 dpf, a time point at which embryonic melanophore development is complete (Hultman et al., 2009), no difference in melanophore number along the lateral stripe was observed (supplementary material Fig. S13A,B,G), indicating that the melanophores develop normally in *nf1* mutants. To assess the regeneration and metamorphic lineage of melanophores, we suppressed melanin synthesis after 3 dpf by treatment with *N*-phenylthiourea (PTU) (Hultman and Johnson, 2010), which allowed us to identify newly formed melanophores by their melanin-negative and pale appearance (supplementary material Fig. S13C,D, red arrows). Removal of PTU at 5 dpf restored melanin synthesis and regeneration and metamorphic melanophores appeared

melanin-positive by 6 dpf (supplementary material Fig. S13E,F, black arrows). The abnormal appearance of the lateral stripes in mutant larvae can be attributed to defects in patterning of regeneration and metamorphic melanophores (supplementary material Fig. S13F,G, brackets), suggesting abnormal migration or differentiation of this lineage. Head melanophore numbers at 6 dpf were not significantly changed in *nf1* mutant larvae and sibling controls (supplementary material Fig. S14). Collectively, these data demonstrate a specific defect in lateral stripe melanophore numbers following *nf1* allele loss, most prominent in the setting of biallelic *nf1a*/*nf1b* loss. Each *nf1a*$^{-/-}$; *nf1b*$^{-/-}$ larvae showed a unique pattern of lateral stripe melanophore loss, suggesting a stochastic defect in melanophore differentiation from neural crest, proliferation, migration or survival, rather than a defect specific to any particular somite of the developing embryo and larvae.

DISCUSSION

NF1 is a common tumor-predisposing, autosomal dominant genetic disorder characterized by café-au-lait macules and cutaneous neurofibromas. In addition to these pigmentation defects and tumors of the peripheral nervous system (PNS), NF1 patients demonstrate highly diversified clinical features with multiple tissue types affected. Prominent lesions include optic pathway gliomas, Lisch nodules, skeletal dysplasia, cardiovascular abnormalities, learning defects and various cancers such as leukemia and intestinal tumors (Side et al., 1997; Side et al., 1998; Bahuau et al., 2000; Andersson et al., 2005; Williams et al., 2009). It remains unclear how *NF1* mutations contribute to the diverse symptoms and tissue types affected in patients. Because neurofibromin is a very large protein that is highly conserved evolutionarily, it is likely to have activities related to functional domains other than those affecting Ras signaling. For example, in addition to Ras, neurofibromin can bind to microtubules, syndecan, phospholipids and amyloid precursor protein (Xu and Gutmann, 1997; Hsueh et al., 2001; D'Angelo et al., 2006; De Schepper et al., 2006). Intriguingly, recent studies indicate that neurofibromin might function as a positive regulator of adenylyl cyclase (Guo et al., 2000; Tong et al., 2002; Dasgupta et al., 2003). This function of neurofibromin modulates neuronal differentiation (Hegedus et al., 2007), suggesting the possibility that cognitive defects in NF1 patients might be related to defects in cAMP signaling rather than activated Ras. Furthermore, the tremendous clinical variability in the phenotypic spectrum seen among families with the same molecular *NF1* lesion posits the role of unlinked modifier loci in regulating the expressivity of disease characteristics (Easton et al., 1993; Sabbagh et al., 2009). Nevertheless, the identification of specific modifier genes and the relative contributions of Ras signaling versus other neurofibromin-regulated pathways for specific phenotypes have yet to be fully elucidated. The zebrafish model that we have developed offers an attractive tool for furthering this analysis because it is amenable to small molecule screens, genetic modifier screens and genetic rescue experiments.

A hallmark feature of human NF1 is the presence of pigmentation defects known as café-au-lait spots. Little is known about the underlying mechanisms responsible for this abnormality, and pigmentation abnormalities in other animal models of NF1 have not been described. In this regard, it is of interest that zebrafish lacking neurofibromin exhibit abnormal patterning of the melanophores that compose the lateral stripes, a phenotype similar to that following pharmacologic inhibition of the upstream Ras effector ErbB (Hultman et al., 2009; Hultman and Johnson, 2010). This easily observable and quantifiable phenotype offers the opportunity to probe underlying molecular pathways modulated by *nf1* in melanophores.

Several studies employing murine models have previously shown a role for neurofibromin in regulating cell numbers of CNS OPCs and astrocytes as well as PNS Schwann cells and sympathetic neurons (Brannan et al., 1994; Gutmann et al., 1999; Bennett et al., 2003; Zhu et al., 2005b; Hegedus et al., 2007; Zheng et al., 2008). These are consistent with our findings in *nf1a/nf1b* mutants and indicative of a strong evolutionary conservation of Nf1 function in neural development. Our observation of impaired compact myelin formation and reduced CNS *plp1a* expression with unperturbed CNS and increased PNS *mbp* expression suggests that the differentiation programs of oligodendrocytes and Schwann cells respond differently to Nf1 deficiency. Alternatively, the observed ultrastructural defects in myelinated CNS axons might arise secondary to neuronal defects. The accessibility of the zebrafish embryo to mosaic analysis offers the ability to differentiate between these possibilities. Unlike *Nf1*-deficient mice, however, *nf1a*/*nf1b* mutant radial glia failed to demonstrate an appreciable increase in Gfap expression. Instead, we observed a decrease in Blbp expression and irregularities in patterning of *nf1a*$^{-/-}$; *nf1b*$^{-/-}$ radial glial cells. This discrepancy might reflect species-specific differences in neural tissue as opposed to Nf1 function, because it remains unclear whether zebrafish radial glia-like ependymal cells are functionally equivalent to mammalian astrocytes.

We have previously characterized cardiovascular defects resulting from morpholino knockdown of *nf1a* and *nf1b* in zebrafish (Padmanabhan et al., 2009; Lee et al., 2010). These defects were observed at 48 and 72 hpf and probably resulted from impairment of both maternal and zygotic gene expression. In our stable compound mutants, we observed partially penetrant insufficiency of the atrioventricular valve at 3 dpf along with significant edema and impaired blood circulation associated with irregular heart rates beginning at 5-6 dpf (data not shown). However, we could not determine whether these effects were primary or secondary. It is possible that impaired cardiac function is the cause of death of these larvae. The absence of earlier cardiovascular phenotypes is most probably due to the activity of maternal transcripts (Abrams and Mullins, 2009); confirmation of this interpretation awaits the creation of a maternal zygotic mutation.

Ubiquitous and conditional *Nf1* knockout mice have been generated to investigate the role of neurofibromin in development and tumorigenesis (Cichowski and Jacks, 2001; Le and Parada, 2007). Conditional loss of *Nf1* with *p53* deficiency in mice results in the development of grade III and IV astrocytomas with full penetrance (Zhu et al., 2005a), indicating that *Nf1* mutations are associated not only with low-grade but also high-grade astrocytoma. Indeed, two independent studies have demonstrated that *NF1* mutations are found in about 15-23% of human glioblastoma multiformes (GBMs) (Parsons et al., 2008; The Cancer Genome Atlas Research Network, 2008). Interestingly, we also observed gliomas in zebrafish lacking *nf1* and *p53*. Likewise, MPNSTs are observed in both mouse and zebrafish models. Thus, the relative advantages of murine and zebrafish systems can be

leveraged for future studies aimed at developing therapeutics for these lethal complications of NF1.

In summary, we have developed and characterized zebrafish lines containing specific targeted mutations in *nf1a* and *nf1b*. Compound deficiency of *nf1a* and *nf1b* results in lethality and predisposes to tumor formation. These studies provide a powerful new tool for analysis of neurofibromin function and for the development of therapies for a common human disorder.

METHODS

Zebrafish lines

The *nf1a*$^{\Delta 5}$, *nf1a*$^{\Delta 8}$, *nf1b*$^{+10}$ and *nf1b*$^{\Delta 55}$ mutant alleles were generated by application of modularly assembled ZFNs. The *nf1a*^{L1247X} mutant allele was generated by TILLING. Our *nf1* mutant alleles were crossed into various transgenic lines, including Tg(*gfap:GFP*) (Lam et al., 2009), Tg(*sox10:GFP*) (Thermes et al., 2002; Carney et al., 2006) and Tg(*olig2:GFP*) (Shin et al., 2003), as well as the *p53*$^{e7/e7}$ mutant line (Berghmans et al., 2005). Zebrafish were maintained under standard conditions as previously described (Westerfield, 2000). All experiments involving animals were approved by the Institutional Animal Care and Use Committees of Harvard University and the University of Pennsylvania.

TILLING with screening by CEL-I method

Individual samples from a preconstructed 'live library' of pooled genomic DNA from ENU-mutagenized F1 animals were used as a template for PCR with the following PCR primer pairs: nf1a_outer_F, 5′-TGGCAAATAAATGCTGACAGA-3′ and nf1a_inner_F, 5′-HEX-TTTTTATATCTCATGTTTAGCTCACAA-3′; nf1a_outer_R, 5′-AAGTCTTAAATGGCCTGAGTGG-3′ and nf1a_inner_R, 5′-6FAM-AAATGGCCTGAGTGGTAATAAA-3′. A nested PCR was performed first using the outer primer pair with the following PCR conditions: 94°C for 2 minutes; 30 cycles of 94°C for 30 seconds, 60°C for 40 seconds and 72°C for 1 minute; and 72°C for 5 minutes. Amplification was then performed using the inner primer pair with the following PCR conditions: 94°C for 2 minutes; 25 cycles of 94°C for 30 seconds, 60°C for 40 seconds and 72°C for 1 minute; and 72°C for 5 minutes. PCR products were denatured, allowed to re-anneal, subjected to CEL-I digestion and separated by acrylamide electrophoresis using a LI-COR DNA analyzer. Upon identification of a genomic DNA sample harboring a mutation in the analyzed region, the individual animals comprising that genomic DNA pool were rescreened to identify the appropriate F1 animal harboring the lesion of interest. This F1 animal was then outcrossed to wild-type fish and progeny were selected on the basis of the presence of the desired mutation. A genotyping strategy was developed to identify animals harboring the nonsense allele isolated by our TILLING strategy using the following PCR primers: nf1a_stop_PstI_F, 5′-CTCTCTTCGACTCTCGCCATCTGCTGTATCAGCTGC-3′ and nf1a_stop_R, 5′-GAAGCAGAAGGTCATAATCTTGCTGGCTAGGC-3′. PCR conditions were 95°C for 2 minutes; 32 cycles of 94°C for 30 seconds, 62°C for 30 seconds and 72°C for 30 seconds; and 72°C for 5 minutes. This generates a 134 bp PCR product. The wild-type allele is resistant to PCR digestion by *Pst*I, but the mutant allele is not.

Modular assembly of ZFNs

The desired three finger zinc finger proteins (ZFPs) were constructed by a splice overlap extension PCR strategy, with individual finger modules amplified from a archive of ZFPs with defined DNA-binding specificities (Zhu et al., 2011). Three individual fingers (F1, F2 and F3) were amplified using primers specific to their desired backbone position, followed by an overlapping PCR step to place them together into a single ZFP fragment which was cloned, sequence verified and subsequently subcloned in frame with a *Fok*I nuclease variant in a pCS2 expression plasmid. The primers for the three backbone positions were as follows: F1 forward, 5′-GCGATGGGTACCCGCCCATATGCTTGC-3′ and F1 reverse, 5′-CACTGGAAGGGCTTCTGGCCTGTGTGAATCCGGATGTG-3′; F2 forward, 5′-CATCCGGATTCACACAGGCCAGAAGCCCTTCCAGTGTCGCATCTGC-3′ and F2 reverse, 5′-ATGTCGCATGCAAAAGGCTTCTCGCCTGTGTGGGTGCGGATGTG-3′; F3 forward, 5′-CGAGAAGCCTTTTGCATGCGACA-3′ and F3 reverse, 5′-GCGTAGGATCCACCTGTGTGGATCTTGGTGTG-3′. The PCR conditions for amplifying F1 were 98°C for 2 minutes and 15 cycles of 94°C for 30 seconds, 68°C for 30 seconds and 72°C for 20 seconds. The PCR conditions for F2 and F3 were 98°C for 2 minutes and 20 cycles of 94°C for 30 seconds, 57°C for 30 seconds and 72°C for 30 seconds. The three individual gel-purified PCR products for positions F1, F2 and F3 were combined (15 ng of each) in a PCR using Advantage 2 HiFi polymerase (Clontech) and subjected to the thermal cycling of 94°C for 2 minutes and five cycles of 94°C for 30 seconds, 55°C for 30 seconds and 72°C for 30 seconds. Following this cycling program, F1 forward and F3 reverse primers were added to the reaction and thermal cycling was continued as follows: 25 cycles of 94°C for 15 seconds and 68°C for 30 seconds. This PCR product of approximately 300 bp was gel-purified, cloned, sequence verified and subcloned in frame with the DD/RR or EL/KK *Fok*I variants (Miller et al., 2007; Szczepek et al., 2007) with and without the 3′-UTR of *nanos1* (Koprunner et al., 2001).

ZFN mRNA injections and genotyping assays

We utilized protocols similar to those recently described (Zhu et al., 2011). pCS2-based expression plasmids containing our constructed ZFNs were linearized downstream of the SV40 polyadenylation signal and used as templates for in vitro transcription of *ZFN* mRNAs (Ambion). One-cell fertilized zebrafish embryos were injected with varying amounts of DD/RR or EL/KK *Fok*I variant mRNAs. Site-specific ZFN function was verified by a genotyping strategy wherein introduction of mutagenic lesions at the target site leads to loss of a unique endogenous restriction site. This same strategy was later used to genotype F1 animals. For *nf1a* and *nf1b*, PCR was performed using the following primer pairs and PCR conditions: *nf1a* F genotyping primer, 5′-GGTGTGTATGTAAATGGGCTCAATG-3′; *nf1a* R genotyping primer, 5′-TACAGTTTCCATAAAACCTGACATTTC-3′; *nf1b* F genotyping primer, 5′-TGCTACCTGCCGGCAGGCTCAG-3′; and *nf1b* R genotyping primer, 5′-ACCTGTGACCATCATGTTACTGACA-3′. PCR conditions for *nf1a* were 94°C for 2 minutes; 35 cycles of 94°C for 30 seconds, 54.8°C for 30 seconds and 72°C for 40 seconds; and 72°C for 5 minutes. PCR conditions for *nf1b* were 94°C for 2 minutes; 35 cycles of 94°C for 30 seconds,

62°C for 30 seconds and 72°C for 40 seconds; and 72°C for 5 minutes. For both *nf1a* and *nf1b*, a 223-bp PCR product was generated. Mutant alleles were resistant to subsequent digestion with *Bsp*CNI or *Dde*I (*nf1a*) and *Bsl*I or *Eco*NI (*nf1b*), whereas the wild-type alleles were completely digested. The molecular identities of the various mutant alleles were determined by cloning and sequencing the restriction enzyme-resistant PCR products from individual embryos derived from outcrosses of F1 animals to wild-type fish.

Larval genotyping

A modified fin clip genotyping strategy was utilized to identify larval genotypes prior to sacrifice. Briefly, 2-dpf larvae were anesthetized with tricaine and stereomicroscopic amputation was performed on the caudal fin with an angled dissecting knife (Fine Science Tools, 10056-12). Genomic DNA from fin-clipped tissue samples was prepared by collecting specimens in 1.5 µl of the surrounding medium and dispensing into PCR tubes containing 7.5 µl of 60 mM NaOH, which were incubated at 95°C for 20 minutes followed by 4°C for 5 minutes with the subsequent addition of 1 µl of 1 M Tris-HCl pH 8. Genotyping for *nf1a* or *nf1b* was performed as described with an increase in PCR cycle number to 40. Genomic DNA prepared by this strategy was sufficient for a single genotyping reaction. Thus, parental crosses were selected to ensure all progeny were homozygous for the non-genotyped *nf1* allele (e.g. $nf1a^{+/-}$; $nf1b^{-/-}$ incross). This was verified by genotyping the homozygous mutant allele in sibling clutchmates.

Whole-mount in situ hybridization and TUNEL staining, immunohistochemistry and BrdU labeling

Antisense RNA probes were generated for *plp1a* (Park et al., 2002) and *mbp* (Lyons et al., 2005) using a digoxigenin RNA labeling kit (Roche). A previously published protocol (Thisse and Thisse, 2008) was followed with minor modifications. Terminal deoxynucleotidyl transferase dUTP nick-end labeling (TUNEL) staining of larvae was performed using the ApopTag Peroxidase In Situ Apoptosis Detection Kit (EMD Millipore) with minor modifications. Larvae were subsequently blocked in 2% blocking reagent (Roche) for 4 hours at room temperature and incubated overnight in anti-digoxigenin-POD antibody (Roche; 1:500) at 4°C. TUNEL-positive cells were detected using the TSA fluorescein system (PerkinElmer). Apoptotic cells were quantified by counting TUNEL-positive cells between somites 6 and 15. For immunohistochemical analysis of zebrafish larvae, we used mouse anti-BrdU (Developmental Studies Hybridoma Bank G3G4; 1:1000), mouse anti-HuC/D (Invitrogen A-21271; 1:100), mouse anti-pERK1/2 (Sigma; 1:200), mouse anti-Zrf1 (Zebrafish International Resource Center; 1:1000), rabbit anti-BLBP (Millipore AB9558; 1:1000), rabbit anti-pS6 (Cell Signaling 2211; 1:200), and rabbit anti-SOX10 (Park et al., 2005) (a generous gift from Bruce Appel, University of Colorado, Denver, CO; 1:5000) as primary antibodies. For fluorescent detection of antibody labeling, we used anti-mouse and anti-rabbit IgG antibodies conjugated with Alexa Fluor 488, 568 and 647 (Invitrogen; 1:200). Immunohistochemistry of adult zebrafish tumor samples was performed according to a previously published protocol (Ligon et al., 2004). Primary antibodies included anti-pERK1/2 (Cell Signaling 4370; 1:200), anti-pS6 (Cell Signaling 2211; 1:50), anti-phosphorylated histone H3 (Cell Signaling 9706; 1:100), rabbit anti-SOX10 (Park et al., 2005) (1:3000), mouse anti-GFAP (Sigma G3893; 1:10,000), anti-HuC/D (Invitrogen A-21271; 1:200) and anti-synaptophys (Millipore MAB5258; 1:1000). Antibody binding was detected using a diaminobenzidine-peroxidase visualization system (EnVision+, Dako). Mayer's hematoxylin was used for counterstaining. For BrdU labeling, embryos were incubated in BrdU solution (10 mM BrdU in 2% DMSO) for 12 hours. After BrdU incubation, embryos were fixed with 4% paraformaldehyde and embedded in 1.5% agarose. Sections from embedded frozen specimens were immersed in 2 M HCl for 15 minutes and processed for immunohistochemistry. Paraffin sectioning followed by hematoxylin and eosin (H&E) staining was performed at the Dana-Farber/Harvard Cancer Center Research Pathology Core.

Behavioral analysis

Startle behavioral experiments were performed on 5-dpf larvae raised as previously described (Burgess and Granato, 2007b). Larvae with underinflated swim bladders were excluded from behavioral testing. Acoustic startle responses were elicited and measured as previously described (Burgess and Granato, 2007a; Wolman et al., 2011), such that larvae could be tracked and analyzed individually. All startle stimuli were 1000 Hz waveforms of 3 milliseconds duration at an intensity of approximately 150 m/second^2. Stimulus intensity was calculated by measuring the displacement of the testing arena due to vibration. To evaluate short latency C-start (SLC) behavior, images were recorded 30 milliseconds prior to and 90 milliseconds following the delivery of the 3 millisecond acoustic stimulus. To examine acoustic startle larval motor behaviors, we captured video recordings using a MotionPro high-speed camera (Redlake) at 1000 frames per second with 512×512 pixel resolution using a 50 mm macro lens. Behavioral analyses were carried out with the FLOTE software package (Burgess and Granato, 2007b; Burgess and Granato, 2007a). Startle short-term habituation was performed and analyzed as previously described (Wolman et al., 2011). Larvae were genotyped following behavioral testing.

Western blotting

Protein lysates were prepared from 3-dpf wild-type, $nf1a^{-/-}$; $nf1b^{+/+}$, $nf1a^{+/+}$; $nf1b^{-/-}$ and $nf1a^{-/-}$; $nf1b^{-/-}$ larvae. Briefly, groups of 10-20 larvae with identical genotype were anesthetized with tricaine, deyolked in a solution of ice-cold PBS with 0.1% Tween-20 (PBST), transferred to a pre-chilled microcentrifuge tube containing 5 µl of lysis buffer (150 mM NaCl, 50 mM Tris-HCl pH 8, 5 mM EDTA, 1 mM PMSF, 1% Igepal CA 630, 0.5% sodium deoxycholate, 0.1% SDS and 1× Halt protease inhibitor cocktail (Thermo Fisher Scientific) per larva, sonicated using a Bioruptor (Diagenode) and cleared by centrifugation. Larval (100 µg) and 293T (25 µg) protein lysates were separated by gel electrophoresis, transferred to PVDF membranes and probed overnight at 4°C with the following primary antibodies: anti-neurofibromin (Abcam ab17963; 1:1000), anti-α-tubulin (Sigma T6074; 1:1000), anti-pERK1/2 (Cell Signaling 4377; 1:1000), and anti-ERK1/2 (Cell Signaling 9102; 1:1000). Primary antibody binding was visualized on X-ray film using anti-mouse-HRP (Cell Signaling 7076; 1:10,000) or anti-rabbit-HRP (Cell Signaling 7074; 1:10,000) secondary antibodies along with LumiGLO (Cell Signaling) or SuperSignal West Femto (Thermo Fisher Scientific) chemiluminescent substrates. Each Western blot was performed in three independent replicates with a representative image of one presented.

Quantification of lateral line and head melanophores

Lateral stripe melanophores, including those observed along the horizontal myoseptum, were counted by a blinded observer in live progeny from *nf1a*$^{+/-}$; *nf1b*$^{+/-}$ incrosses at 3 and 6 dpf. Each discrete melanized region was counted as a single melanophore. Following 6-dpf lateral stripe melanophore quantitation, larvae were immersed in E3 medium containing 5 mg/ml epinephrine (Sigma E4375) for 10 minutes to induce contraction of melanosomes around cell bodies and allow evaluation of head melanophore numbers. Larvae were fixed overnight in 4% paraformaldehyde in PBS at 4°C, washed twice with PBS for 5 minutes, and melanophores anterior to somite one across the crown of the head (supplementary material Fig. S14) were counted. Larvae were subsequently genotyped for *nf1a* and *nf1b*. Data analysis was performed by one-way ANOVA with Dunnett's post-test (GraphPad InStat 3.1a, GraphPad Software).

Serial tracking of lateral line melanophores

Lateral stripe melanophores of live progeny from *nf1a*$^{+/-}$; *nf1b*$^{-/-}$ or wild-type incrosses were individually imaged at 3 dpf followed by incubation with 0.2 mM *N*-phenylthiourea (PTU, Sigma) to prevent melanin synthesis. At 5 dpf, lateral stripe melanophores were again imaged, after which PTU was washed out. Larvae were reimaged at 6 dpf and subsequently genotyped for *nf1a*. Images were acquired using a Nikon SMZ1500 microscope and NIS-Elements F2.20 software with identical settings. Melanophores in a 200-µm region, corresponding to roughly 12 somites at 3 dpf, were counted at 3 and 6 dpf for each larva. Statistical analysis was performed using a one-tail, unpaired *t*-test (GraphPad Prism 5, GraphPad Software).

Intestinal transit assays

Groups of 5-dpf wild-type and *nf1a*$^{-/-}$; *nf1b*$^{-/-}$ larvae were placed in individual wells of six-well plates containing feeding medium [4 ml E3, 2 ml paramecia culture and 5 µl of 2-µm yellow-green microspheres (Polysciences 18338)]. Larvae were incubated at 28.5°C for 1 hour followed by several E3 washes. Individual larvae were transferred to 24-well plates and visually assessed for the presence of fluorescent microspheres in the intestinal bulb. Extent of intestinal transit was observed at 2, 4, 6 and 24 hours. Transit was considered to be complete when fluorescence was no longer detectable in the intestinal tract.

Transmission electron microscopy

TEM was carried out at the Harvard Medical School Electron Microscopy Facility. Briefly, embryos were fixed in 2% formaldehyde and 2.5% glutaraldehyde, post-fixed with 1% osmium tetroxide and embedded in epon. Sections were collected in the trunk region of embryos. Images were captured by a Tecnai G^2 Spirit BioTWIN electron microscope with an AMT 2k CCD camera.

Tumor identification

nf1a$^{\Delta 8/+}$; *nf1b*$^{+10/+10}$; *p53*$^{e7/e7}$ fish were incrossed and progeny were manually evaluated weekly for 45 weeks. Animals identified as having tumors were separated and fin-clipped for genotyping purposes. These samples were subsequently subjected to histological and immunohistochemical analyses as described above for determination of tumor type. At the completion of 45 weeks, all tumor-free fish were genotyped for subsequent statistical analysis.

TRANSLATIONAL IMPACT

Clinical issue

Neurofibromatosis type 1 (NF1) is one of the most commonly inherited human genetic disorders. Despite nearly complete penetrance, the clinical expression of NF1 varies widely, even within families harboring identical mutations at the *NF1* locus. Not surprisingly, few genotype-phenotype relationships have thus far been reported for NF1, suggesting important contributions from unlinked modifier genes and/or environmental factors. However, these observations do not preclude mutations or deletions within the *NF1* locus from influencing pathology. Instead, they highlight the need for better experimental tools to address this important and clinically relevant observation. Additional models of NF1 are needed to begin elucidating these mechanisms using scalable chemical and genetic approaches.

Results

The authors employ zinc finger nucleases and TILLING to isolate null alleles of the two zebrafish orthologues of human *NF1*, *nf1a* and *nf1b*. They report that zebrafish lacking *nf1a* and *nf1b* exhibit valvular insufficiency, defects in learning and behavior and early larval lethality. Larvae carrying a single wild-type allele of either *nf1a* or *nf1b* are viable and fertile, suggesting functional redundancy. The authors also observe hyperplasia and aberrant differentiation in the oligodendrocyte progenitor cells and Schwann cells populating the nervous systems of *nf1*-null larvae. This is accompanied by irregularities in the myelin sheaths surrounding the neuronal axons of the central nervous system. Human *NF1* is a potent tumor-suppressor gene and the authors provide evidence that zebrafish *nf1a* and *nf1b* function similarly: they demonstrate that Ras is hyperactivated in the spinal cords of *nf1*-null larvae, and that the combined loss of *nf1* and *p53* accelerates tumorigenesis. Finally, the authors characterize a melanophore defect resulting from *nf1* loss that disrupts the uniform pigmentation pattern observed along the lateral stripes.

Implications and future directions

Using zebrafish to probe the genetic, epistatic and environmental factors underlying NF1 pathology offers several important advantages over currently available murine models. The low costs and high fecundity of zebrafish coupled with their ability to survive for several days as haploid organisms make them amenable to large-scale genetic screens. Thus, *nf1*-deficient zebrafish should greatly facilitate the identification of modifier genes influencing NF1 pathogenesis. In addition, genetic rescue experiments using specific *NF1* mutations or deletions could clarify the molecular basis of pathology. The feasibility of high-throughput chemical screening using this model should provide additional valuable mechanistic insights and identify lead compounds for future therapeutics. Few treatment options are currently available for individuals affected with NF1, so advances in this area are urgently needed. Importantly, this represents the first animal model that demonstrates pigmentation defects analogous to the pathognomonic café-au-lait spots seen in affected individuals. Therefore, this model will provide a platform for further investigation of one of the most common clinical pathologies associated with NF1.

ACKNOWLEDGEMENTS

We thank members of the Epstein and Look laboratories for helpful discussions, especially Rajan Jain and Nikhil Singh. We are grateful to Jie He for her expert assistance with zebrafish husbandry; Michael Pack and Mary Mullins for thoughtful suggestions; Joshua Abrams, Jesse Isaacman-Beck and Allison Rosenberg for technical instruction; and Thomas Joseph for critical reading of the manuscript.

COMPETING INTERESTS

The authors declare that they do not have any competing or financial interests.

AUTHOR CONTRIBUTIONS

J.S., A.P., E.D.D., M.A.W., J.P.K., N.D.L., S.A.W., K.L.L, J.A.E. and A.T.L. conceived and designed the experiments. J.S., A.P., E.D.D., J-S.L., S.H., S.D., F.G. and M.A.W. performed the experiments. J.S., A.P., E.D.D., J.P.K., K.L.L., J.A.E. and A.T.L. analyzed the data. M.G., N.D.L., S.A.W., S-H.K., L.S-K. and K.L.L. contributed reagents, materials and analysis tools. A.P., J.S., E.D.D., J.P.K., A.T.L. and J.A.E. wrote the paper.

FUNDING

This work was supported by the Department of Defense [grant numbers W81XWH-07-1-0228 and W81XWH-12-1-0125 to J.A.E. and A.T.L.] and the National Institutes of Health [grant numbers R01 HL062974 to J.A.E.; R01 HL093766 to N.D.L. and S.A.W.; T32 HL007843-15 to E.D.D.; and R01 HG002995 to L.S.-K.). A.T.L. was supported by an Innovator Award from Alex's Lemonade Stand Foundation. A.P. was supported by a fellowship from the Sarnoff Cardiovascular Research Foundation, J.S. was supported by a fellowship from the Dana-Farber Cancer Institute (DFCI) Pediatric Low-Grade Astrocytoma Program, and J.-S.L. was supported by a Young Investigator Award from the Children's Tumor Foundation. This work was also supported by the Vanderbilt University Academic Venture Capital Fund to L.S.-K. as well as the Spain Fund for Regenerative Medicine and the W.W. Smith Endowed Chair to J.A.E.

SUPPLEMENTARY MATERIAL

Supplementary material for this article is available at http://dmm.biologists.org/lookup/suppl/doi:10.1242/dmm.009779/-/DC1

REFERENCES

Abrams, E. W. and Mullins, M. C. (2009). Early zebrafish development: it's in the maternal genes. *Curr. Opin. Genet. Dev.* **19**, 396-403.

Amores, A., Force, A., Yan, Y. L., Joly, L., Amemiya, C., Fritz, A., Ho, R. K., Langeland, J., Prince, V., Wang, Y. L. et al. (1998). Zebrafish hox clusters and vertebrate genome evolution. *Science* **282**, 1711-1714.

Andersson, J., Sihto, H., Meis-Kindblom, J. M., Joensuu, H., Nupponen, N. and Kindblom, L. G. (2005). NF1-associated gastrointestinal stromal tumors have unique clinical, phenotypic, and genotypic characteristics. *Am. J. Surg. Pathol.* **29**, 1170-1176.

Bahuau, M., Laurendeau, I., Pelet, A., Assouline, B., Lamireau, T., Taine, L., Le Bail, B., Vergnes, P., Gallet, S., Vidaud, M. et al. (2000). Tandem duplication within the neurofibromatosis type 1 gene (NF1) and reciprocal t(15;16)(q26.3;q12.1) translocation in familial association of NF1 with intestinal neuronal dysplasia type B (IND B). *J. Med. Genet.* **37**, 146-150.

Bannykh, S. I., Stolt, C. C., Kim, J., Perry, A. and Wegner, M. (2006). Oligodendroglial-specific transcriptional factor SOX10 is ubiquitously expressed in human gliomas. *J. Neurooncol.* **76**, 115-127.

Bennett, M. R., Rizvi, T. A., Karyala, S., McKinnon, R. D. and Ratner, N. (2003). Aberrant growth and differentiation of oligodendrocyte progenitors in neurofibromatosis type 1 mutants. *J. Neurosci.* **23**, 7207-7217.

Berghmans, S., Murphey, R. D., Wienholds, E., Neuberg, D., Kutok, J. L., Fletcher, C. D., Morris, J. P., Liu, T. X., Schulte-Merker, S., Kanki, J. P. et al. (2005). tp53 mutant zebrafish develop malignant peripheral nerve sheath tumors. *Proc. Natl. Acad. Sci. USA* **102**, 407-412.

Brannan, C. I., Perkins, A. S., Vogel, K. S., Ratner, N., Nordlund, M. L., Reid, S. W., Buchberg, A. M., Jenkins, N. A., Parada, L. and Copeland, N. G. (1994). Targeted disruption of the neurofibromatosis type-1 gene leads to developmental abnormalities in heart and various neural crest-derived tissues. *Genes Dev.* **8**, 1019-1029.

Burgess, H. A. and Granato, M. (2007a). Sensorimotor gating in larval zebrafish. *J. Neurosci.* **27**, 4984-4994.

Burgess, H. A. and Granato, M. (2007b). Modulation of locomotor activity in larval zebrafish during light adaptation. *J. Exp. Biol.* **210**, 2526-2539.

Carney, T. J., Dutton, K. A., Greenhill, E., Delfino-Machin, M., Dufourcq, P., Blader, P. and Kelsh, R. N. (2006). A direct role for Sox10 in specification of neural crest-derived sensory neurons. *Development* **133**, 4619-4630.

Cawthon, R. M., Weiss, R., Xu, G. F., Viskochil, D., Culver, M., Stevens, J., Robertson, M., Dunn, D., Gesteland, R., O'Connell, P. et al. (1990). A major segment of the neurofibromatosis type 1 gene: cDNA sequence, genomic structure, and point mutations. *Cell* **62**, 193-201.

Cichowski, K. and Jacks, T. (2001). NF1 tumor suppressor gene function: narrowing the GAP. *Cell* **104**, 593-604.

Cichowski, K., Shih, T. S., Schmitt, E., Santiago, S., Reilly, K., McLaughlin, M. E., Bronson, R. T. and Jacks, T. (1999). Mouse models of tumor development in neurofibromatosis type 1. *Science* **286**, 2172-2176.

D'Angelo, I., Welti, S., Bonneau, F. and Scheffzek, K. (2006). A novel bipartite phospholipid-binding module in the neurofibromatosis type 1 protein. *EMBO Rep.* **7**, 174-179.

Dasgupta, B., Dugan, L. L. and Gutmann, D. H. (2003). The neurofibromatosis 1 gene product neurofibromin regulates pituitary adenylate cyclase-activating polypeptide-mediated signaling in astrocytes. *J. Neurosci.* **23**, 8949-8954.

Dasgupta, B., Yi, Y., Chen, D. Y., Weber, J. D. and Gutmann, D. H. (2005). Proteomic analysis reveals hyperactivation of the mammalian target of rapamycin pathway in neurofibromatosis 1-associated human and mouse brain tumors. *Cancer Res.* **65**, 2755-2760.

De Schepper, S., Boucneau, J. M., Westbroek, W., Mommaas, M., Onderwater, J., Messiaen, L., Naeyaert, J. M. and Lambert, J. L. (2006). Neurofibromatosis type 1 protein and amyloid precursor protein interact in normal human melanocytes and colocalize with melanosomes. *J. Investig. Dermatol.* **126**, 653-659.

Ducatman, B. S., Scheithauer, B. W., Piepgras, D. G., Reiman, H. M. and Ilstrup, D. M. (1986). Malignant peripheral nerve sheath tumors. A clinicopathologic study of 120 cases. *Cancer* **57**, 2006-2021.

Easton, D. F., Ponder, M. A., Huson, S. M. and Ponder, B. A. (1993). An analysis of variation in expression of neurofibromatosis (NF) type 1 (NF1): evidence for modifying genes. *Am. J. Hum. Genet.* **53**, 305-313.

Eliyahu, D., Raz, A., Gruss, P., Givol, D. and Oren, M. (1984). Participation of p53 cellular tumour antigen in transformation of normal embryonic cells. *Nature* **312**, 646-649.

Guo, H. F., Tong, J., Hannan, F., Luo, L. and Zhong, Y. (2000). A neurofibromatosis-1-regulated pathway is required for learning in Drosophila. *Nature* **403**, 895-898.

Gutmann, D. H., Loehr, A., Zhang, Y., Kim, J., Henkemeyer, M. and Cashen, A. (1999). Haploinsufficiency for the neurofibromatosis 1 (NF1) tumor suppressor results in increased astrocyte proliferation. *Oncogene* **18**, 4450-4459.

Hegedus, B., Dasgupta, B., Shin, J. E., Emnett, R. J., Hart-Mahon, E. K., Elghazi, L., Bernal-Mizrachi, E. and Gutmann, D. H. (2007). Neurofibromatosis-1 regulates neuronal and glial cell differentiation from neuroglial progenitors in vivo by both cAMP- and Ras-dependent mechanisms. *Cell Stem Cell* **1**, 443-457.

Hirose, T., Scheithauer, B. W. and Sano, T. (1998). Perineurial malignant peripheral nerve sheath tumor (MPNST): a clinicopathologic, immunohistochemical, and ultrastructural study of seven cases. *Am. J. Surg. Pathol.* **22**, 1368-1378.

Hsueh, Y. P., Roberts, A. M., Volta, M., Sheng, M. and Roberts, R. G. (2001). Bipartite interaction between neurofibromatosis type I protein (neurofibromin) and syndecan transmembrane heparan sulfate proteoglycans. *J. Neurosci.* **21**, 3764-3770.

Hultman, K. A. and Johnson, S. L. (2010). Differential contribution of direct-developing and stem cell-derived melanocytes to the zebrafish larval pigment pattern. *Dev Biol.* **337**, 425-431.

Hultman, K. A., Budi, E. H., Teasley, D. C., Gottlieb, A. Y., Parichy, D. M. and Johnson, S. L. (2009). Defects in ErbB-dependent establishment of adult melanocyte stem cells reveal independent origins for embryonic and regeneration melanocytes. *PLoS Genet.* **5**, e1000544.

Hundley, J. E., Koester, S. K., Troyer, D. A., Hilsenbeck, S. G., Subler, M. A. and Windle, J. J. (1997). Increased tumor proliferation and genomic instability without decreased apoptosis in MMTV-ras mice deficient in p53. *Mol. Cell. Biol.* **17**, 723-731.

Jacks, T., Shih, T. S., Schmitt, E. M., Bronson, R. T., Bernards, A. and Weinberg, R. A. (1994). Tumour predisposition in mice heterozygous for a targeted mutation in Nf1. *Nat. Genet.* **7**, 353-361.

Kemp, C. J., Burns, P. A., Brown, K., Nagase, H. and Balmain, A. (1994). Transgenic approaches to the analysis of ras and p53 function in multistage carcinogenesis. *Cold Spring Harb. Symp. Quant. Biol.* **59**, 427-434.

Koprunner, M., Thisse, C., Thisse, B. and Raz, E. (2001). A zebrafish nanos-related gene is essential for the development of primordial germ cells. *Genes Dev.* **15**, 2877-2885.

Lam, C. S., Marz, M. and Strahle, U. (2009). gfap and nestin reporter lines reveal characteristics of neural progenitors in the adult zebrafish brain. *Dev. Dyn.* **238**, 475-486.

Le, L. Q. and Parada, L. F. (2007). Tumor microenvironment and neurofibromatosis type I: connecting the GAPs. *Oncogene* **26**, 4609-4616.

Lee, J. S., Padmanabhan, A., Shin, J., Zhu, S., Guo, F., Kanki, J. P., Epstein, J. A. and Look, A. T. (2010). Oligodendrocyte progenitor cell numbers and migration are regulated by the zebrafish orthologs of the NF1 tumor suppressor gene. *Hum. Mol. Genet.* **19**, 4643-4653.

Ligon, K. L., Alberta, J. A., Kho, A. T., Weiss, J., Kwaan, M. R., Nutt, C. L., Louis, D. N., Stiles, C. D. and Rowitch, D. H. (2004). The oligodendroglial lineage marker OLIG2 is universally expressed in diffuse gliomas. *J. Neuropathol. Exp. Neurol.* **63**, 499-509.

Lyons, D. A., Pogoda, H. M., Voas, M. G., Woods, I. G., Diamond, B., Nix, R., Arana, N., Jacobs, J. and Talbot, W. S. (2005). erbb3 and erbb2 are essential for schwann cell migration and myelination in zebrafish. *Curr. Biol.* **15**, 513-524.

Miller, J. C., Holmes, M. C., Wang, J., Guschin, D. Y., Lee, Y. L., Rupniewski, I., Beausejour, C. M., Waite, A. J., Wang, N. S., Kim, K. A. et al. (2007). An improved zinc-finger nuclease architecture for highly specific genome editing. *Nat. Biotechnol.* **25**, 778-785.

Padmanabhan, A., Lee, J. S., Ismat, F. A., Lu, M. M., Lawson, N. D., Kanki, J. P., Look, A. T. and Epstein, J. A. (2009). Cardiac and vascular functions of the zebrafish orthologues of the type I neurofibromatosis gene NFI. *Proc. Natl. Acad. Sci. USA* **106**, 22305-22310.

Parada, L. F., Land, H., Weinberg, R. A., Wolf, D. and Rotter, V. (1984). Cooperation between gene encoding p53 tumour antigen and ras in cellular transformation. *Nature* **312**, 649-651.

Park, H. C., Mehta, A., Richardson, J. S. and Appel, B. (2002). olig2 is required for zebrafish primary motor neuron and oligodendrocyte development. *Dev. Biol.* **248**, 356-368.

Park, H. C., Boyce, J., Shin, J. and Appel, B. (2005). Oligodendrocyte specification in zebrafish requires notch-regulated cyclin-dependent kinase inhibitor function. *J. Neurosci.* **25**, 6836-6844.

Parsons, D. W., Jones, S., Zhang, X., Lin, J. C., Leary, R. J., Angenendt, P., Mankoo, P., Carter, H., Siu, I. M., Gallia, G. L. et al. (2008). An integrated genomic analysis of human glioblastoma multiforme. *Science* **321**, 1807-1812.

Powers, J. F., Evinger, M. J., Zhi, J., Picard, K. L. and Tischler, A. S. (2007). Pheochromocytomas in Nf1 knockout mice express a neural progenitor gene expression profile. *Neuroscience* **147**, 928-937.

Sabbagh, A., Pasmant, E., Laurendeau, I., Parfait, B., Barbarot, S., Guillot, B., Combemale, P., Ferkal, S., Vidaud, M., Aubourg, P. et al. (2009). Unravelling the genetic basis of variable clinical expression in neurofibromatosis 1. *Hum. Mol. Genet.* **18**, 2768-2778.

Shin, J., Park, H. C., Topczewska, J. M., Mawdsley, D. J. and Appel, B. (2003). Neural cell fate analysis in zebrafish using olig2 BAC transgenics. *Methods Cell Sci.* **25**, 7-14.

Side, L., Taylor, B., Cayouette, M., Conner, E., Thompson, P., Luce, M. and Shannon, K. (1997). Homozygous inactivation of the NF1 gene in bone marrow cells from children with neurofibromatosis type 1 and malignant myeloid disorders. *N. Engl. J. Med.* **336**, 1713-1720.

Side, L. E., Emanuel, P. D., Taylor, B., Franklin, J., Thompson, P., Castleberry, R. P. and Shannon, K. M. (1998). Mutations of the NF1 gene in children with juvenile myelomonocytic leukemia without clinical evidence of neurofibromatosis, type 1. *Blood* **92**, 267-272.

Szczepek, M., Brondani, V., Buchel, J., Serrano, L., Segal, D. J. and Cathomen, T. (2007). Structure-based redesign of the dimerization interface reduces the toxicity of zinc-finger nucleases. *Nat. Biotechnol.* **25**, 786-793.

Tanaka, M., Omura, K., Watanabe, Y., Oda, Y. and Nakanishi, I. (1994). Prognostic factors of colorectal cancer: K-ras mutation, overexpression of the p53 protein, and cell proliferative activity. *J. Surg. Oncol.* **57**, 57-64.

The Cancer Genome Atlas Research Network. (2008). Comprehensive genomic characterization defines human glioblastoma genes and core pathways. *Nature* **455**, 1061-1068.

Thermes, V., Grabher, C., Ristoratore, F., Bourrat, F., Choulika, A., Wittbrodt, J. and Joly, J. S. (2002). I-SceI meganuclease mediates highly efficient transgenesis in fish. *Mech. Dev.* **118**, 91-98.

Thisse, C. and Thisse, B. (2008). High-resolution in situ hybridization to whole-mount zebrafish embryos. *Nat. Protoc.* **3**, 59-69.

Tong, J., Hannan, F., Zhu, Y., Bernards, A. and Zhong, Y. (2002). Neurofibromin regulates G protein-stimulated adenylyl cyclase activity. *Nat. Neurosci.* **5**, 95-96.

Viskochil, D., Buchberg, A. M., Xu, G., Cawthon, R. M., Stevens, J., Wolff, R. K., Culver, M., Carey, J. C., Copeland, N. G., Jenkins, N. A. et al. (1990). Deletions and a translocation interrupt a cloned gene at the neurofibromatosis type 1 locus. *Cell* **62**, 187-192.

Vogel, K. S., Klesse, L. J., Velasco-Miguel, S., Meyers, K., Rushing, E. J. and Parada, L. F. (1999). Mouse tumor model for neurofibromatosis type 1. *Science* **286**, 2176-2179.

Wallace, M. R., Marchuk, D. A., Andersen, L. B., Letcher, R., Odeh, H. M., Saulino, A. M., Fountain, J. W., Brereton, A., Nicholson, J., Mitchell, A. L. et al. (1990). Type 1 neurofibromatosis gene: identification of a large transcript disrupted in three NF1 patients. *Science* **249**, 181-186.

Wanebo, J. E., Malik, J. M., VandenBerg, S. R., Wanebo, H. J., Driesen, N. and Persing, J. A. (1993). Malignant peripheral nerve sheath tumors. A clinicopathologic study of 28 cases. *Cancer* **71**, 1247-1253.

Westerfield, M. (2000). *The Zebrafish Book: A Guide for the Laboratory Use of Zebrafish (Danio rerio)* (4th edn). Eugene, OR: University of Oregon Press.

Wienholds, E., Schulte-Merker, S., Walderich, B. and Plasterk, R. H. (2002). Target-selected inactivation of the zebrafish rag1 gene. *Science* **297**, 99-102.

Williams, V. C., Lucas, J., Babcock, M. A., Gutmann, D. H., Korf, B. and Maria, B. L. (2009). Neurofibromatosis type 1 revisited. *Pediatrics* **123**, 124-133.

Wolman, M. A., Jain, R. A., Liss, L. and Granato, M. (2011). Chemical modulation of memory formation in larval zebrafish. *Proc. Natl. Acad. Sci. USA* **108**, 15468-15473.

Xu, H. and Gutmann, D. H. (1997). Mutations in the GAP-related domain impair the ability of neurofibromin to associate with microtubules. *Brain Res.* **759**, 149-152.

Zheng, H., Chang, L., Patel, N., Yang, J., Lowe, L., Burns, D. K. and Zhu, Y. (2008). Induction of abnormal proliferation by nonmyelinating schwann cells triggers neurofibroma formation. *Cancer Cell* **13**, 117-128.

Zhu, Y., Guignard, F., Zhao, D., Liu, L., Burns, D. K., Mason, R. P., Messing, A. and Parada, L. F. (2005a). Early inactivation of p53 tumor suppressor gene cooperating with NF1 loss induces malignant astrocytoma. *Cancer Cell* **8**, 119-130.

Zhu, Y., Harada, T., Liu, L., Lush, M. E., Guignard, F., Harada, C., Burns, D. K., Bajenaru, M. L., Gutmann, D. H. and Parada, L. F. (2005b). Inactivation of NF1 in CNS causes increased glial progenitor proliferation and optic glioma formation. *Development* **132**, 5577-5588.

Zhu, C., Smith, T., McNulty, J., Rayla, A. L., Lakshmanan, A., Siekmann, A. F., Buffardi, M., Meng, X., Shin, J., Padmanabhan, A. et al. (2011). Evaluation and application of modularly assembled zinc-finger nucleases in zebrafish. *Development* **138**, 4555-4564.

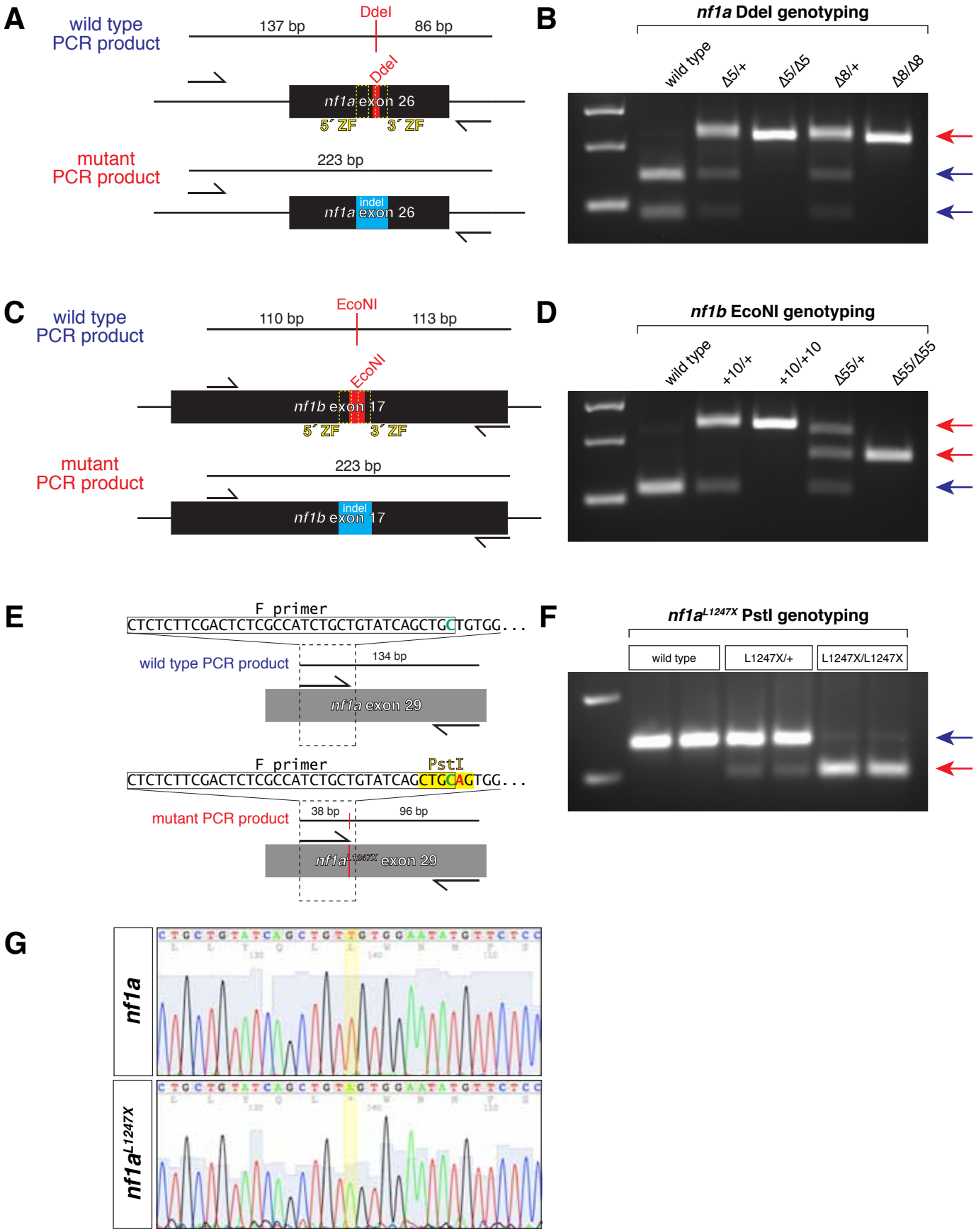

Fig. S1. Genotyping strategies for identification of nf1 mutant alleles.
(A,B) Schematic diagram of PCR products generated from wild type and ZFN-induced mutant *nf1a* alleles (A). The indels (A, blue box) in the Δ8 and Δ5 *nf1a* alleles lead to loss of a native DdeI site, allowing for allelic discrimination by gel electrophoresis of DdeI digested PCR products (B, red arrow, mutant band; blue arrows, wild type bands). (C,D) Schematic diagram of PCR products generated from wild type and ZFN-induced mutant *nf1b* alleles (C). The indels (C, blue box) in the +10 and Δ55 *nf1b* alleles lead to loss of a native EcoNI site, allowing for allelic discrimination by gel electrophoresis of EcoNI digested PCR products (D, red arrows, mutant bands; blue arrow, co-migrating wild type bands). (E,F) Schematic diagram of PCR products generated from wild type and TILLING-induced *nf1a*^{L1247X} alleles (E). The forward primer (F primer) contains a 1 base pair mismatch with the native *nf1a* exon 29 sequence so as to create a PstI restriction site in the mutant, which harbors a T to A nonsense mutation, allowing for allelic discrimination by gel electrophoresis of PstI digested PCR products (F, red arrow, mutant band; blue arrow, wild type band). (G) Sequencing chromatograms from wild type and *nf1a*$^{L1247X/L1247X}$ animals (TILLING-induced mutation highlighted).

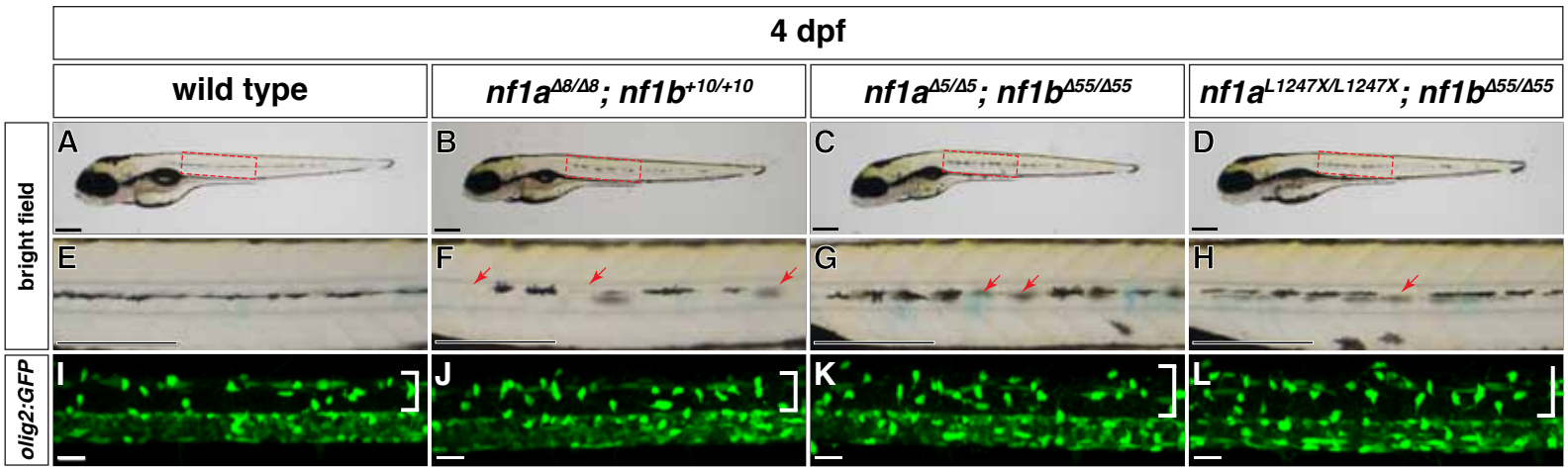

Fig. S2. *nf1*-null mutants with different allelic combinations of *nf1a* and *nf1b* are phenotypically identical. (A-H) Lateral view of wild type (A,E,I), *nf1a*$^{\Delta 8/\Delta 8}$; *nf1b*$^{+10/+10}$ (B,F,J), *nf1a*$^{\Delta 5/\Delta 5}$; *nf1b*$^{\Delta 55/\Delta 55}$ (C,G,K), and *nf1a*$^{L1247X/L1247X}$; *nf1b*$^{+10/+10}$ larvae (D,F,L) at 4 dpf. (E-H) Magnified views of the boxed region in A-D demonstrating absence of melanophores along the lateral line (arrows) in different allelic combinations of *nf1a*; *nf1b* double homozygous mutant alleles. Scale bars: 300 μm. (I-L) Confocal images of spinal cords in Tg(*olig2:GFP*) larvae harboring different allelic combinations of *nf1a*; *nf1b* homozygous mutant alleles at 4 dpf. OPC hyperplasia (brackets) is observed in all three allelic combinations of *nf1a*; *nf1b* double homozygous mutant alleles. Scale bars: 300 μm.

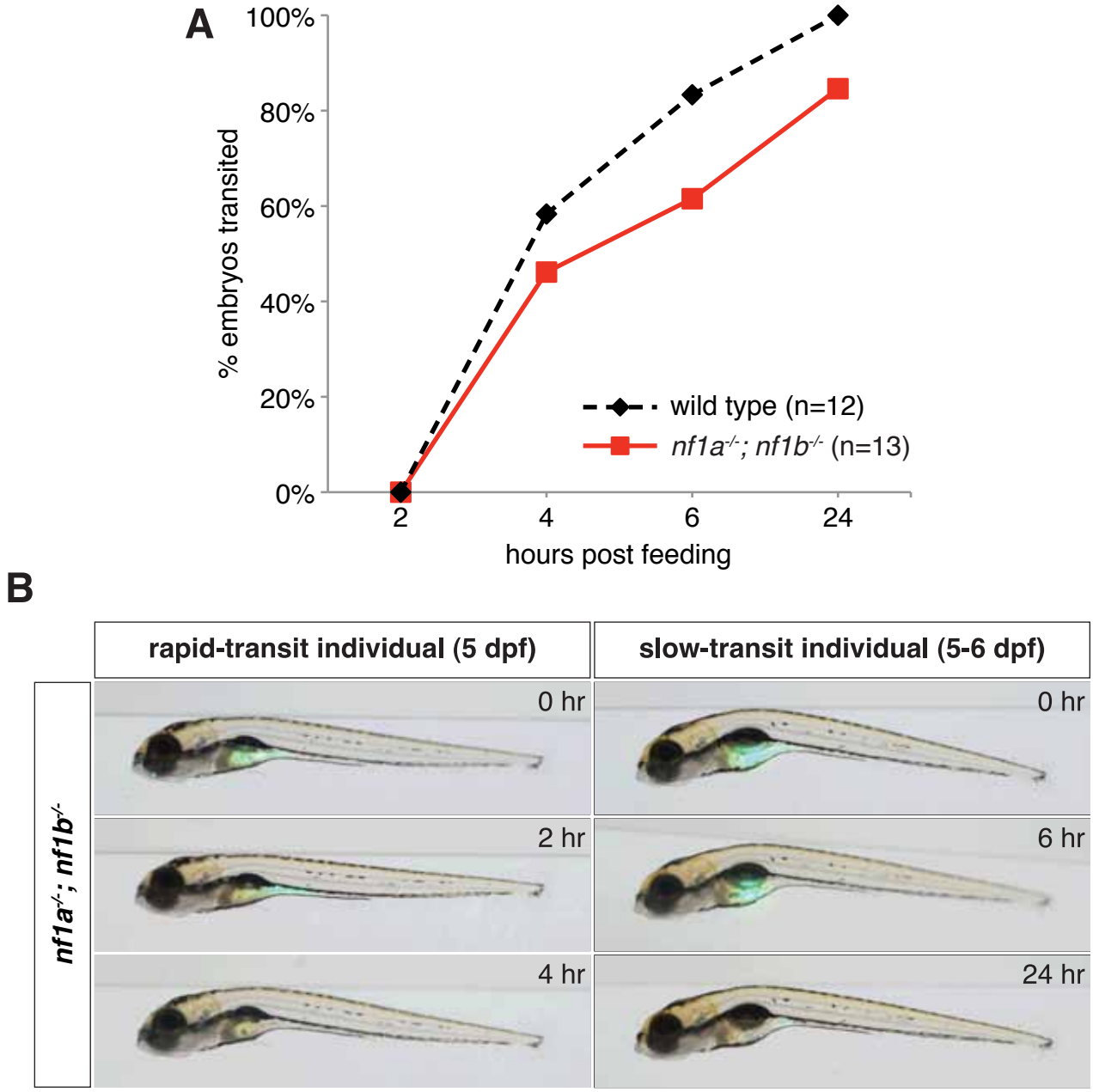

Fig. S3. Loss of *nf1a* and *nf1b* does not affect food consumption or transit.
(A) Graph depicting intestinal transit time for 5 dpf wild type (black line) and *nf1a*$^{-/-}$; *nf1b*$^{-/-}$ (red line) larvae following a 1 hour feeding of paramecia and fluorescent microspheres. Transit was considered to be complete when fluorescent microspheres were no longer detected along the intestinal tract by fluorescent microscopy. (B) Representative overlays of bright field and fluorescent images from 5-6 dpf *nf1a*$^{-/-}$; *nf1b*$^{-/-}$ larvae exhibiting rapid- or slow-transit.

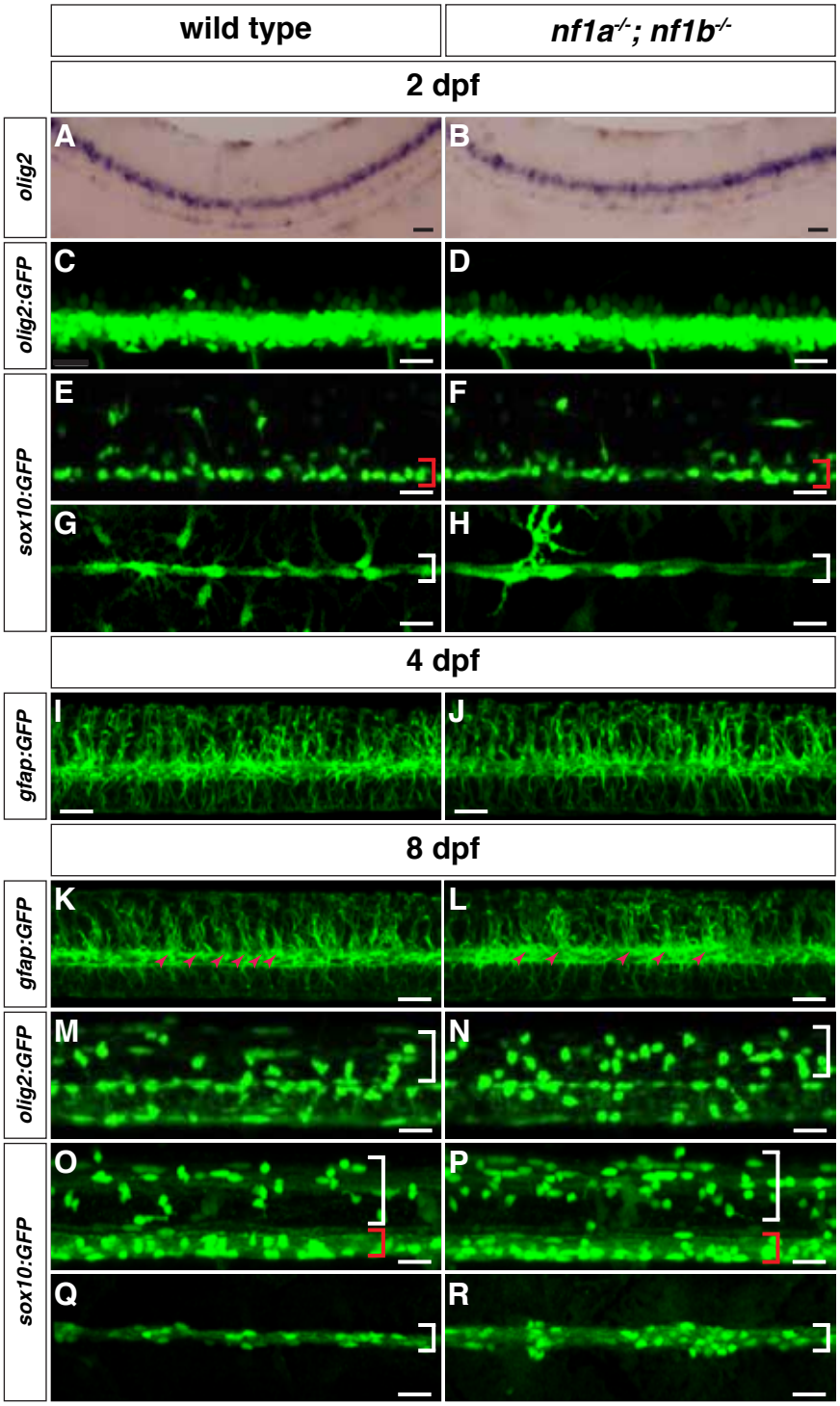

Fig. S4. Analysis of *nf1a*/*nf1b* mutant OPCs and Schwann cells at 2 dpf and radial glia at 4 dpf appear normal with defects appreciated in all three populations at 8 dpf.
(A,B) Whole-mount in situ hybridization for expression of endogenous *olig2* in wild type (A) and *nf1a*$^{-/-}$; *nf1b*$^{-/-}$ (B) larvae at 2 dpf. Scale bars: 20 μm. (C,D) Spinal cord of wild type; Tg(*olig2:GFP*) (C) and *nf1a*$^{-/-}$; *nf1b*$^{-/-}$; Tg(*olig2:GFP*) (D) larvae at 2 dpf. Scale bars: 20 μm. (E,F) Spinal cord of wild type; Tg(*sox10:GFP*) (E) and *nf1a*$^{-/-}$; *nf1b*$^{-/-}$; Tg(*sox10:GFP*) (F) larvae at 2 dpf. Brackets indicate ventrally positioned *sox10*:GFP-positive OPCs. Scale bars: 20 μm. (G,H) PLLn of wild type; Tg(*sox10:GFP*) (G) and *nf1a*$^{-/-}$; *nf1b*$^{-/-}$; Tg(*sox10:GFP*) (H) larvae at 2 dpf. Brackets indicate *sox10*:GFP-positive Schwann cells associated with the PLLn. Scale bars: 20 μm. (I,J) Spinal cord of wild type; Tg(*gfap:GFP*) (I) and *nf1a*$^{-/-}$; *nf1b*$^{-/-}$; Tg(*gfap:GFP*) (J) larvae at 4 dpf. Scale bars: 20 μm. (K,L) Spinal cord of wild type; Tg(*gfap:GFP*) (K) and *nf1a*$^{-/-}$; *nf1b*$^{-/-}$; Tg(*gfap:GFP*) (L) larvae at 8 dpf. Arrowheads depict the normal segmental expression of GFP in wild type larvae (K) that is absent in *nf1a*$^{-/-}$; *nf1b*$^{-/-}$ larvae (L). Scale bars: 20 μm. (M,N) Spinal cord of wild type; Tg(*olig2:GFP*) (M) and *nf1a*$^{-/-}$; *nf1b*$^{-/-}$; Tg(*olig2:GFP*) (N) larvae at 8 dpf. Brackets indicate dorsally positioned *olig2*:GFP-positive OPCs. Scale bars: 20 μm. (O,P) Spinal cord of wild type; Tg(*sox10:GFP*) (O) and *nf1a*$^{-/-}$; *nf1b*$^{-/-}$; Tg(*sox10:GFP*) (P) larvae at 8 dpf. White and red brackets indicate dorsally and ventrally positioned *sox10*:GFP-positive OPCs, respectively. Scale bars: 20 μm. (Q,R) PLLn of wild type; Tg(*sox10:GFP*) (Q) and *nf1a*$^{-/-}$; *nf1b*$^{-/-}$; Tg(*sox10:GFP*) (R) larvae at 8 dpf. Brackets indicate *sox10*:GFP-positive Schwann cells associated with the PLLn. Scale bars: 20 μm.

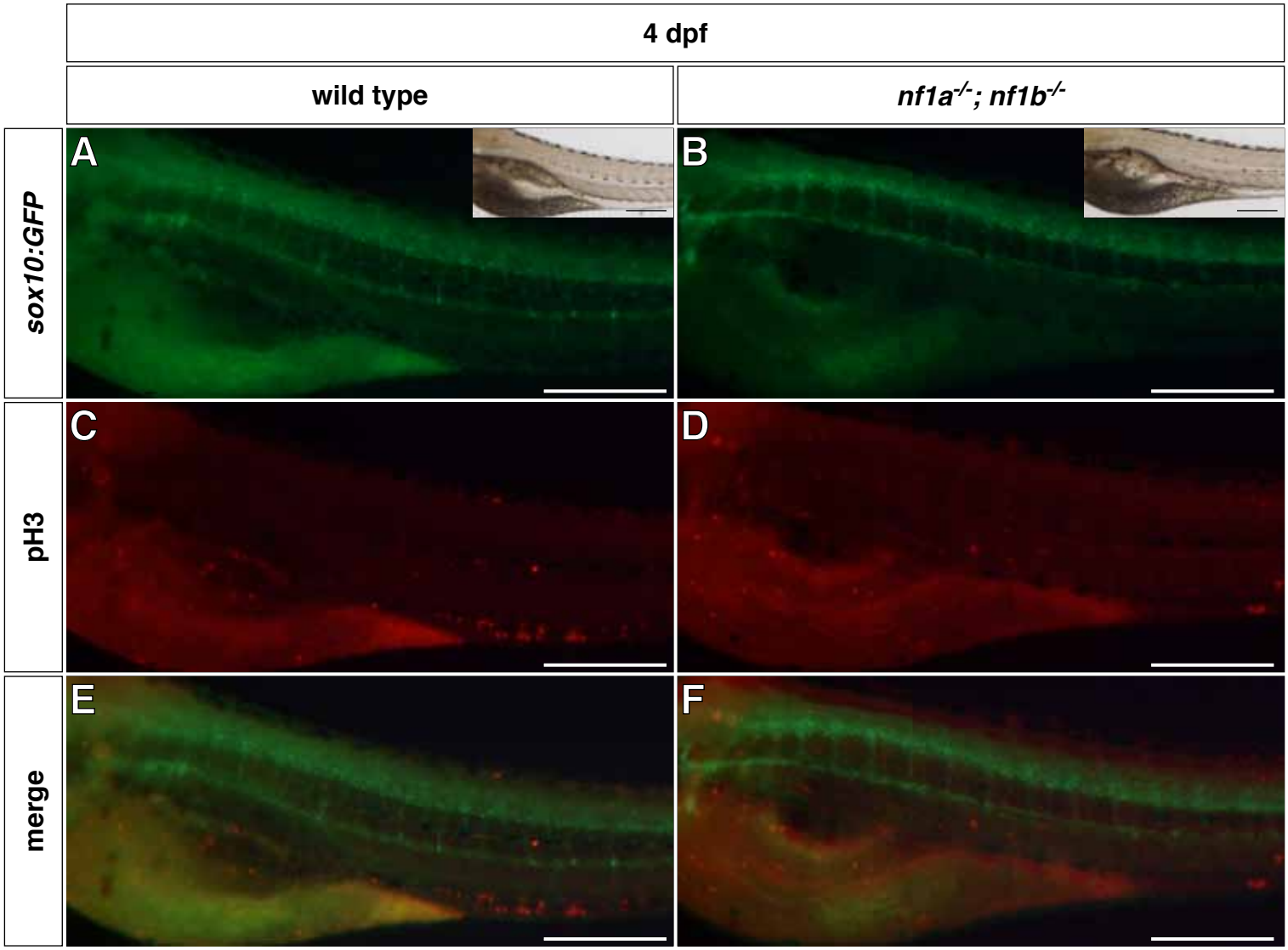

Fig. S5. Increase in posterior lateral line nerve (PLLn) Schwann cell numbers observed in *nf1a*$^{-/-}$; *nf1b*$^{-/-}$ larvae at 4 dpf is not due to increased proliferation.

(A-F) Representative images of transgenic *sox10:GFP* expressing wild type (A,C,E, *n*=13) and *nf1a*$^{-/-}$; *nf1b*$^{-/-}$ (B,D,F, *n*=7) larvae. No increase in phospho-histone H3 (pH3) staining is apparent at 4 dpf in PLLn Schwann cells of *nf1* mutants (D,F) when compared with wild type controls (C,E). Scale bars: 50 μm.

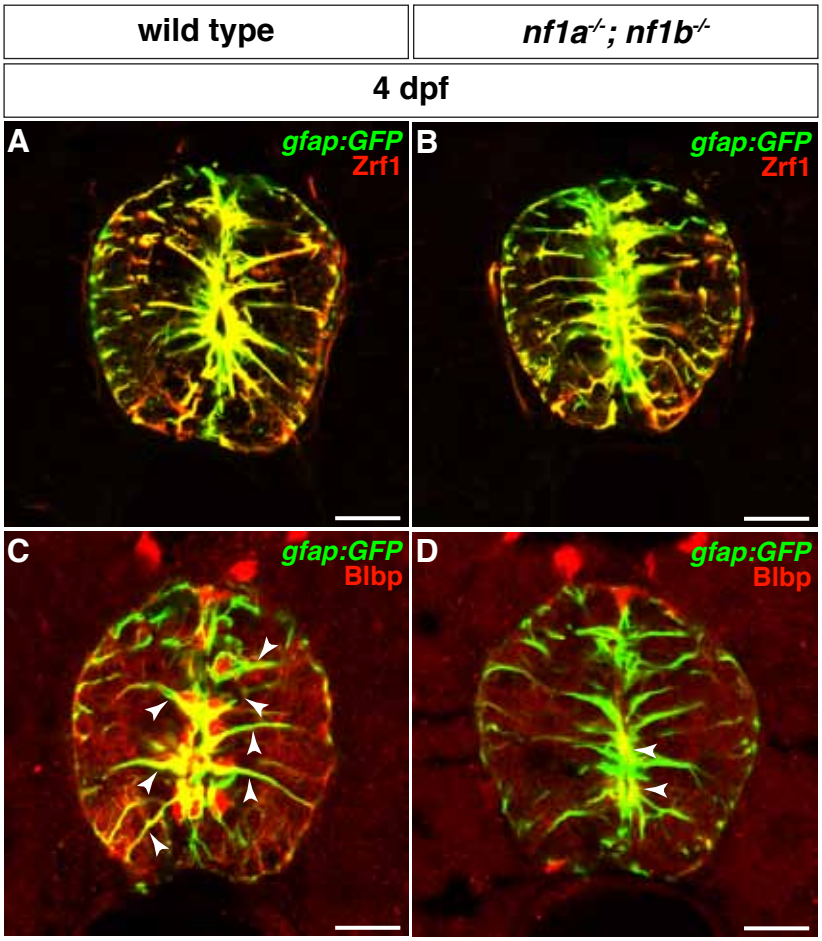

Fig. S6. Radial glia of *nf1a*$^{-/-}$; *nf1b*$^{-/-}$ larvae express reduced amounts of brain lipid binding protein (Blbp). (A,B) Radial glia in transverse sections through the spinal cord of wild type; Tg(*gfap:GFP*) (A) and *nf1a*$^{-/-}$; *nf1b*$^{-/-}$; Tg(*gfap:GFP*) (B) larvae at 4 dpf are marked by expression of the *gfap*:GFP transgene (green) and the Zrf1 antibody (red). (C,D) Radial glia (green) in transverse sections through the spinal cord of *nf1a*$^{-/-}$; *nf1b*$^{-/-}$; Tg(*gfap:GFP*) larvae (D) demonstrate decreased Blbp expression (red), as identified by colocalization (yellow, arrowheads), when compared with wild type; Tg(*gfap:GFP*) larvae (C) at 4 dpf. Scale bars: 20 μm.

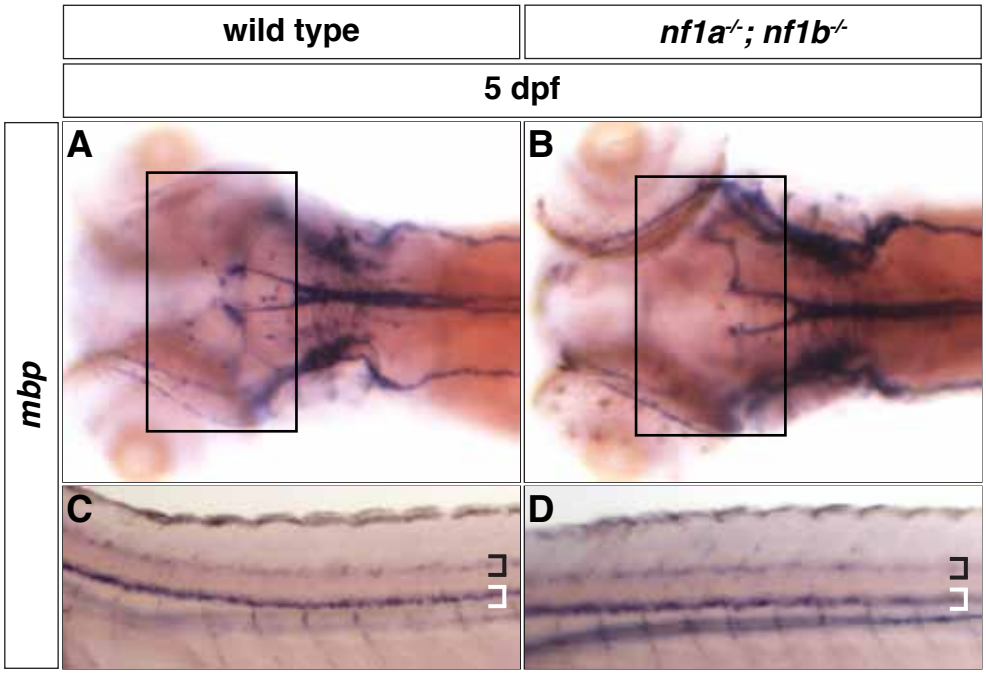

Fig. S7. Expression of *mbp* in the brain and spinal cord of *nf1a*$^{-/-}$; *nf1b*$^{-/-}$ larvae appears normal.
(A,B) No difference in *mbp* expression is appreciated in the midbrain and hindbrain regions (A,B, boxes) as well as along the dorsal (black brackets) and ventral (white brackets) spinal cord of *nf1a*$^{-/-}$; *nf1b*$^{-/-}$ larvae (B,D) when compared to wild type larvae (A,C) by whole mount in situ hybridization at 5 dpf.

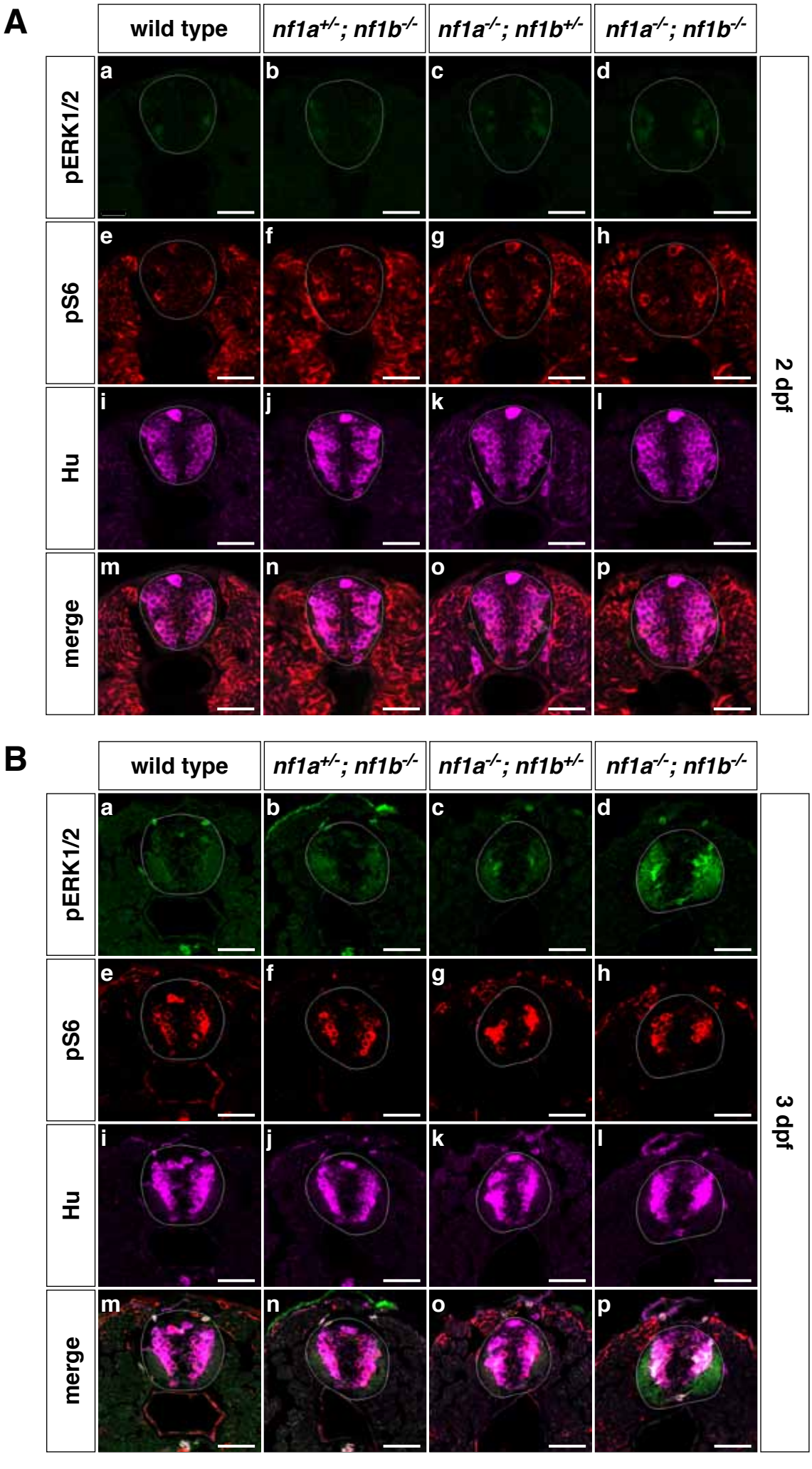

Fig. S8. Increased ERK1/2 phosphorylation is appreciated in the spinal cords of *nf1a*$^{-/-}$; *nf1b*$^{-/-}$ larvae by 3 dpf. Immunohistochemical analysis of transverse sections through the spinal cord of 2 dpf *nf1a*$^{-/-}$; *nf1b*$^{-/-}$ larvae (Ad,Ah,Al,Ap) demonstrates no appreciable differences in pERK1/2 (green) or pS6 staining (red) when compared with *nf1a*$^{+/-}$; *nf1b*$^{-/-}$ (Ab,Af,Aj,An), *nf1a*$^{-/-}$; *nf1b*$^{+/-}$ (Ac,Ag,Ak,Ao), or wild type (Aa,Ae,Ai,Am) larvae. At 3 dpf, however, increased pERK1/2 signal is noted in *nf1a*$^{-/-}$; *nf1b*$^{-/-}$ larvae (Bd,Bp) when compared with *nf1a*$^{+/-}$; *nf1b*$^{-/-}$ (Bb,Bn), *nf1a*$^{-/-}$; *nf1b*$^{+/-}$ (Bc,Bo), or wild type (Ba,Bm) larvae, with no differences noted in levels of pS6 (Be-Bh). Activated ERK1/2 signaling is most prominent in spinal cord neurons, as identified by colocalization (white) with HuC/D expression (magenta) (Bl,Bp). Scale bars: 20 μm.

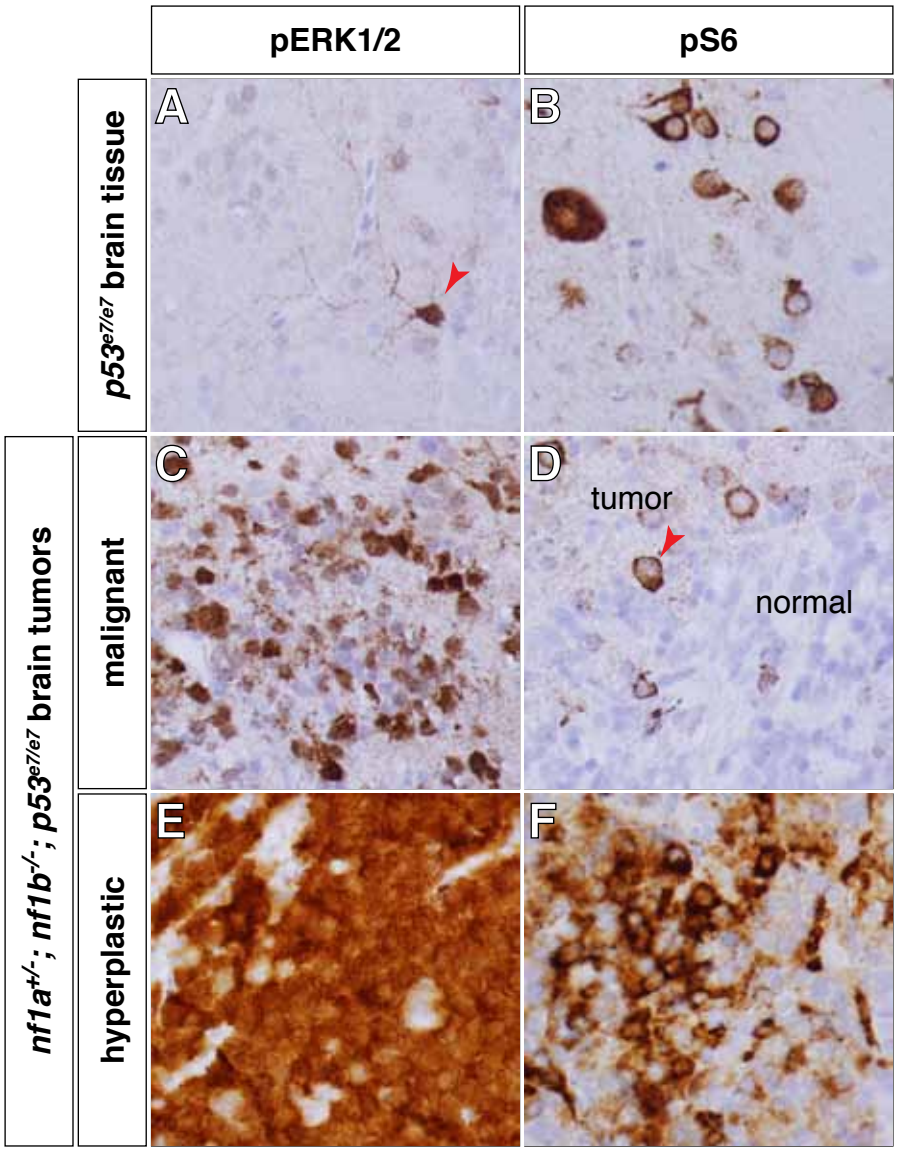

Fig. S9. *nf1a*$^{+/-}$*; nf1b*$^{-/-}$ *;p53*$^{e7/e7}$ brain tumors demonstrate hyperactivation of ERK and mTOR pathways. (A-F) Immunohistochemical analysis of pERK1/2 and pS6 in *p53*$^{e7/e7}$ brain tissue (A,B, red arrow labels normal neuron) as well as *nf1a*$^{+/-}$*; nf1b*$^{-/-}$; *p53*$^{e7/e7}$ brain tumors demonstrating a predominantly malignant (C,D) or hyperproliferative (E,F) phenotype. The more malignant and infiltrative *nf1a*$^{+/-}$*; nf1b*$^{-/-}$; *p53*$^{e7/e7}$ brain tumor demonstrates increased pERK1/2 staining (C), with normal levels of pS6 (D, red arrow labels normal neuron) when compared with similarly stained *p53*$^{e7/e7}$ brain tissue (A,B). The majority of tumor cells in the more hyperplastic *nf1a*$^{+/-}$*; nf1b*$^{-/-}$; *p53*$^{e7/e7}$ brain tumor show staining for pERK1/2 (E) along with heterogeneously increased pS6 (F).

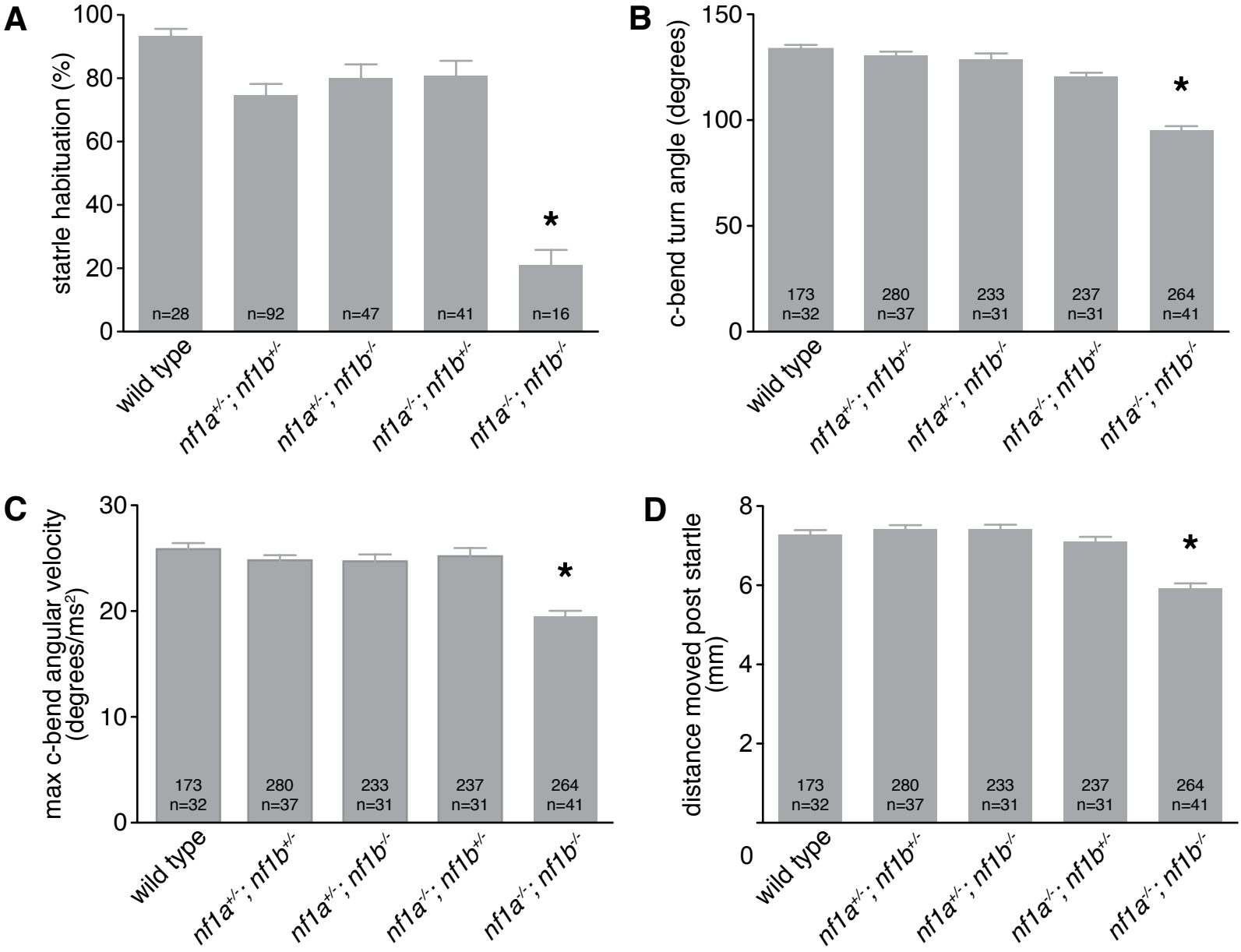

Fig. S10. *nf1a*/*nf1b* mutants exhibit acoustic startle C-start behavioral deficits.
(A) Mean degree of short-term SLC habituation is reduced in 5 dpf *nf1a*$^{-/-}$; *nf1b*$^{-/-}$ larvae. (B-C) Measurement of mean head turning angle (B) and mean maximum angular velocity (C) of initial C-bend following delivery of acoustic stimulus demonstrates a significant reduction of both behavioral measures in 5 dpf *nf1a*$^{-/-}$; *nf1b*$^{-/-}$ larvae. (D) Mean distance traveled over 90 milliseconds following delivery of acoustic stimulus, as a result of short latency C-start behavioral response, is also significantly reduced in 5 dpf *nf1a*$^{-/-}$; *nf1b*$^{-/-}$ larvae. The total number of short latency C-bends and number of larvae tested per genotype appear at the base of each bar graph (*P<0.001).

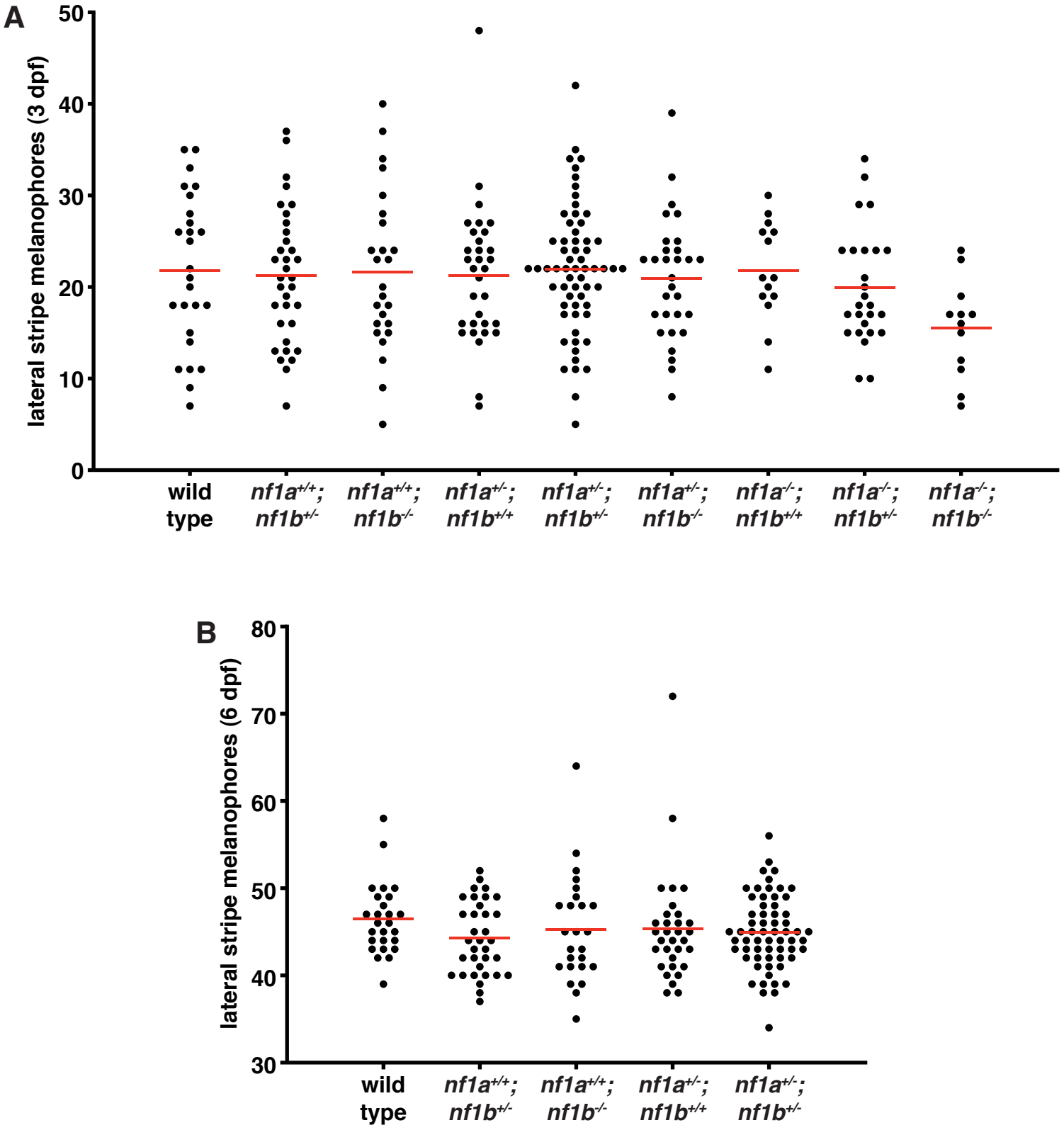

Fig. S11. Quantification of lateral stripe melanophores in wild type and *nf1a*/*nf1b* mutant larvae at 3 and 6 dpf.

(A) Quantification of lateral stripe melanophores from wild type (*n*=26), *nf1a*$^{+/+}$; *nf1b*$^{+/-}$ (*n*=34), *nf1a*$^{+/+}$; *nf1b*$^{-/-}$ (*n*=25), *nf1a*$^{+/-}$; *nf1b*$^{+/+}$ (*n*=32), *nf1a*$^{+/-}$; *nf1b*$^{+/-}$ (*n*=62), *nf1a*$^{+/-}$; *nf1b*$^{-/-}$ (*n*=30), *nf1a*$^{-/-}$; *nf1b*$^{+/+}$ (*n*=14), *nf1a*$^{-/-}$; *nf1b*$^{+/-}$ (*n*=26), and *nf1a*$^{-/-}$; *nf1b*$^{-/-}$ (*n*=12) larvae at 3 dpf. Each point represents the number of lateral stripe melanophores in an individual embryo and red lines indicate mean values. (B) Quantification of lateral stripe melanophores from wild type (*n*=26; same as displayed in Fig. 8), *nf1a*$^{+/+}$; *nf1b*$^{+/-}$ (*n*=34), *nf1a*$^{+/+}$; *nf1b*$^{-/-}$ (*n*=25), *nf1a*$^{+/-}$; *nf1b*$^{+/+}$ (*n*=32), and *nf1a*$^{+/-}$; *nf1b*$^{+/-}$ (*n*=62) larvae at 6 dpf. Each point represents the number of lateral stripe melanophores in an individual embryo and red lines indicate mean values.

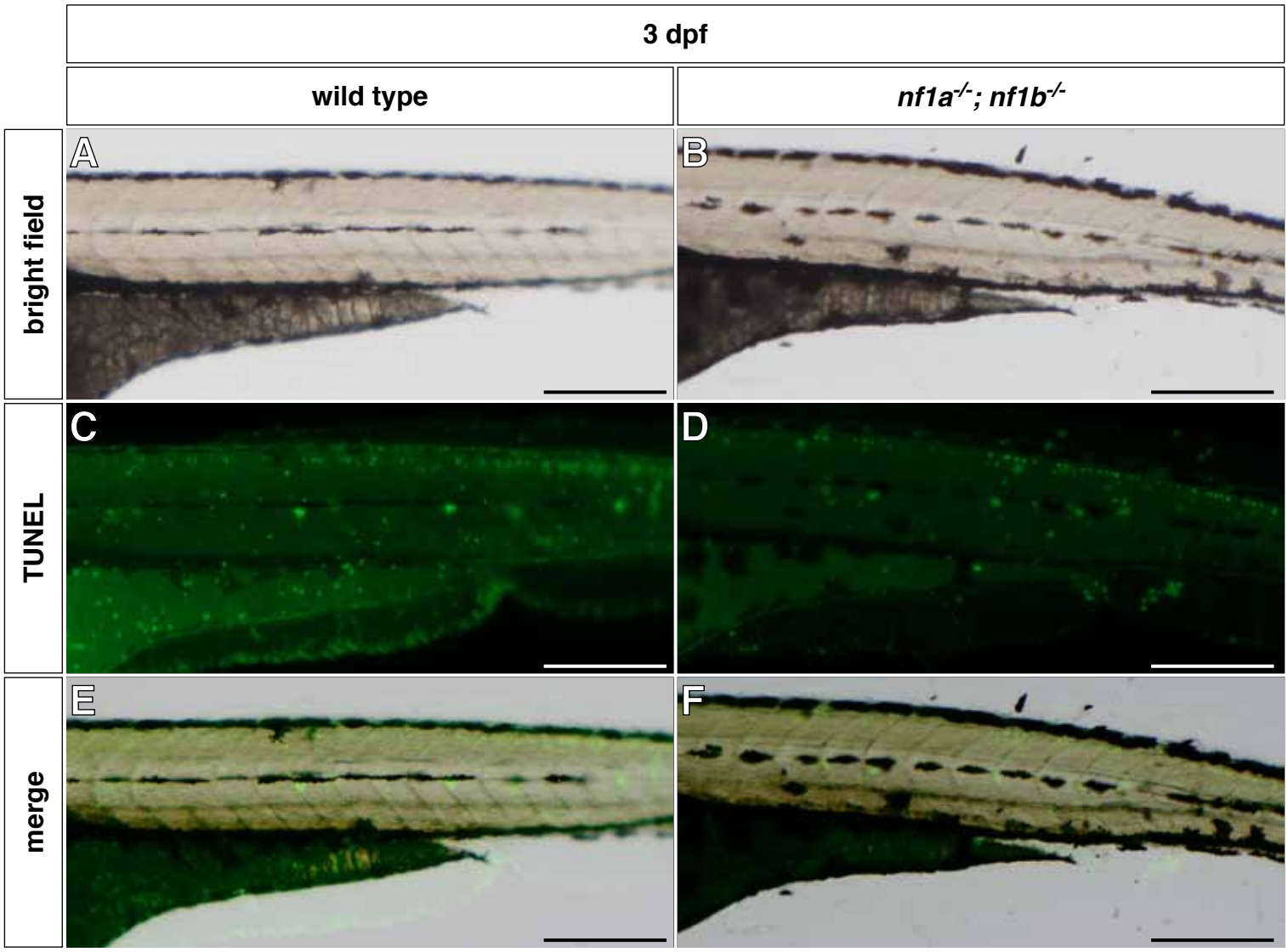

Fig. S12. Melanized embryonic/ontogenetic and unmelanized regeneration and metamorphic melanophores do not demonstrate increased apoptosis at 3 dpf in *nf1a*$^{-/-}$; *nf1b*$^{-/-}$ larvae.
(A-F) Representative images of melanized embryonic/ontogenetic melanophores along the lateral stripe visualized at 3 dpf in wild type (A,C,E) and *nf1a*$^{-/-}$; *nf1b*$^{-/-}$ mutant (B,D,F) larvae. No difference in apoptotic cells was noted (68.1±11 cells/larva, n=12 wild type versus 63.8±8.5, n=12 mutants; P=0.27). No melanized embryonic/ontogenetic cells are noted to be TUNEL-positive in either genotype (C,D), with similar numbers of TUNEL-positive cells appearing in the region where unmelanized regeneration and metamorphic melanophores would be located at this time point (C-F). Scale bars: 50 μm.

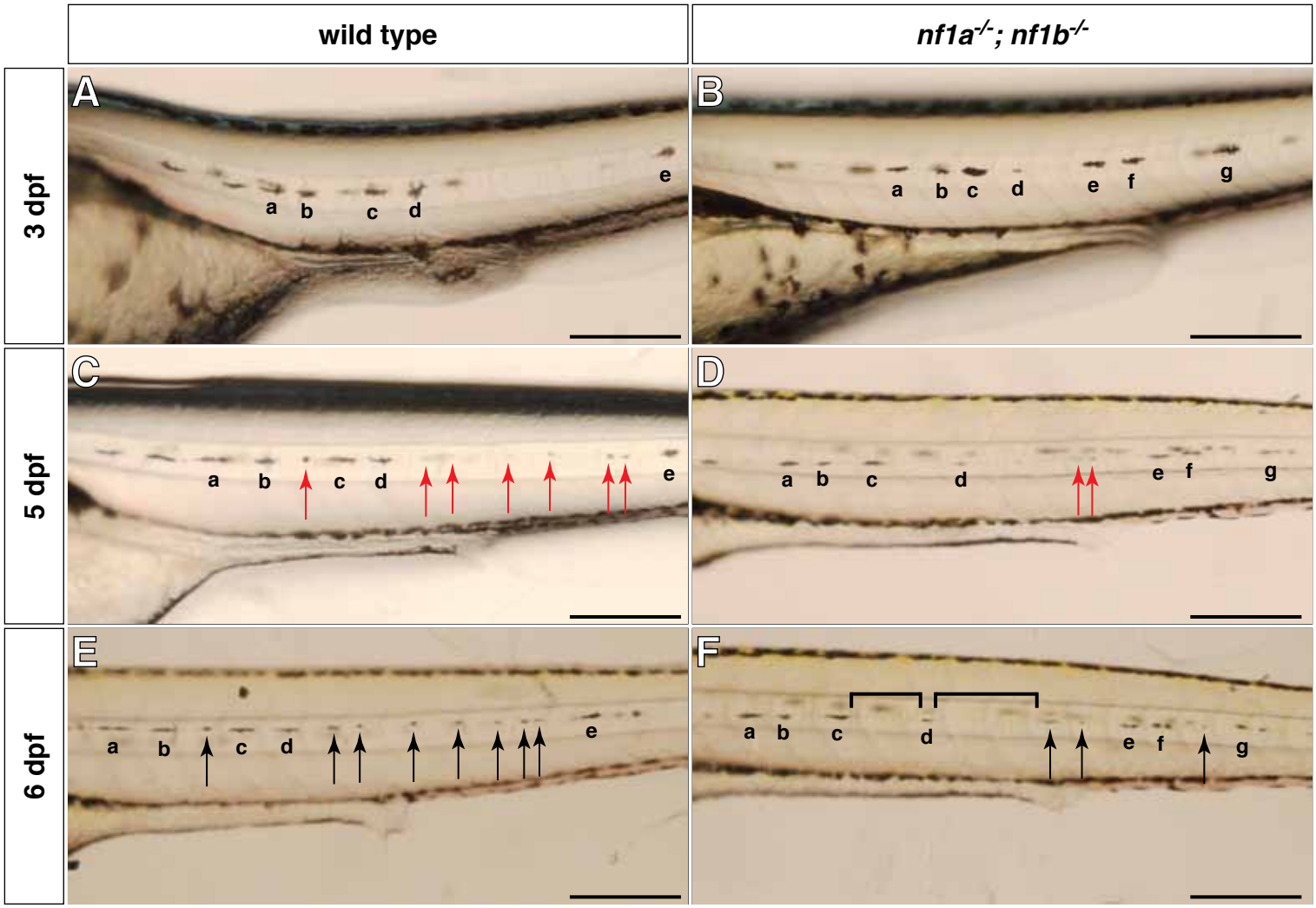

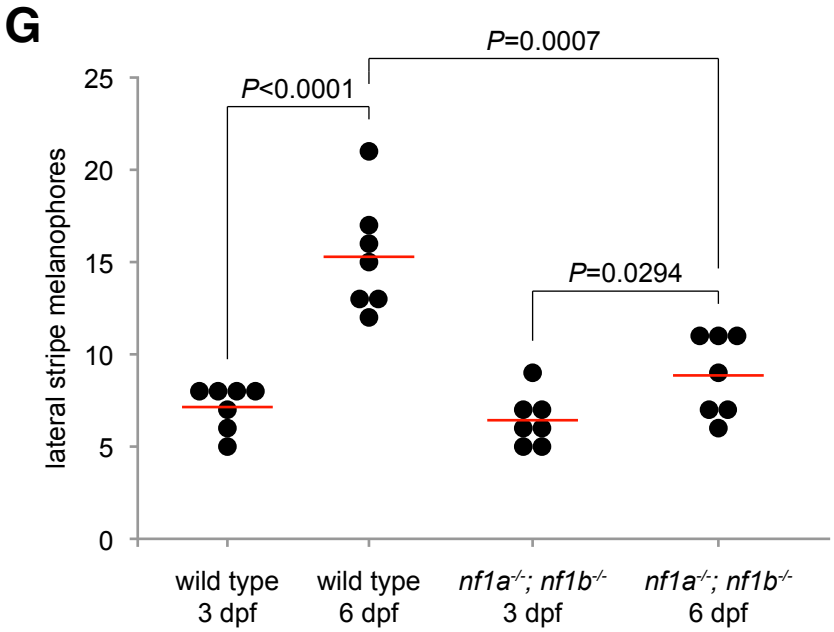

Fig. S13. Gaps in stereotyped pigmentation pattern along the lateral stripe of *nf1a/nf1b* mutants arise from failure of migration or differentiation of the regeneration and metamorphic melanophore lineages.
(A-F) Lateral stripe melanophores were initially imaged at 3 dpf in wild type (A) and *nf1a*$^{-/-}$*; nf1b*$^{-/-}$ (B) larvae, after which these animals were treated with 0.2 mM N-phenylthiourea (PTU) to prevent additional melanin synthesis. Therefore only the embryonic/ontogenetic melanophores melanized before PTU addition remain melanin-positive (C,D, embryonic/ontogenetic melanophores lettered) at 5 dpf. In contrast, the regeneration and metamorphic lineage of melanophores are melanin-negative and appear pale (C,D, red arrows). PTU removal after 5 dpf restores melanin synthesis, evident at 6 dpf when these melanophores become melanin-positive (E,F, black arrows). *nf1a/nf1b* mutants demonstrate gaps (F, brackets) in the pigmentation pattern along the lateral stripe when compared with wild type controls (E). Scale bars: 50 μm. (G) Tracking and quantification of lateral stripe melanophores in a 200 μm segment of the trunk in wild type (n=7) and *nf1a*$^{-/-}$*; nf1b*$^{-/-}$ (n=7) animals at 3 and 6 dpf.

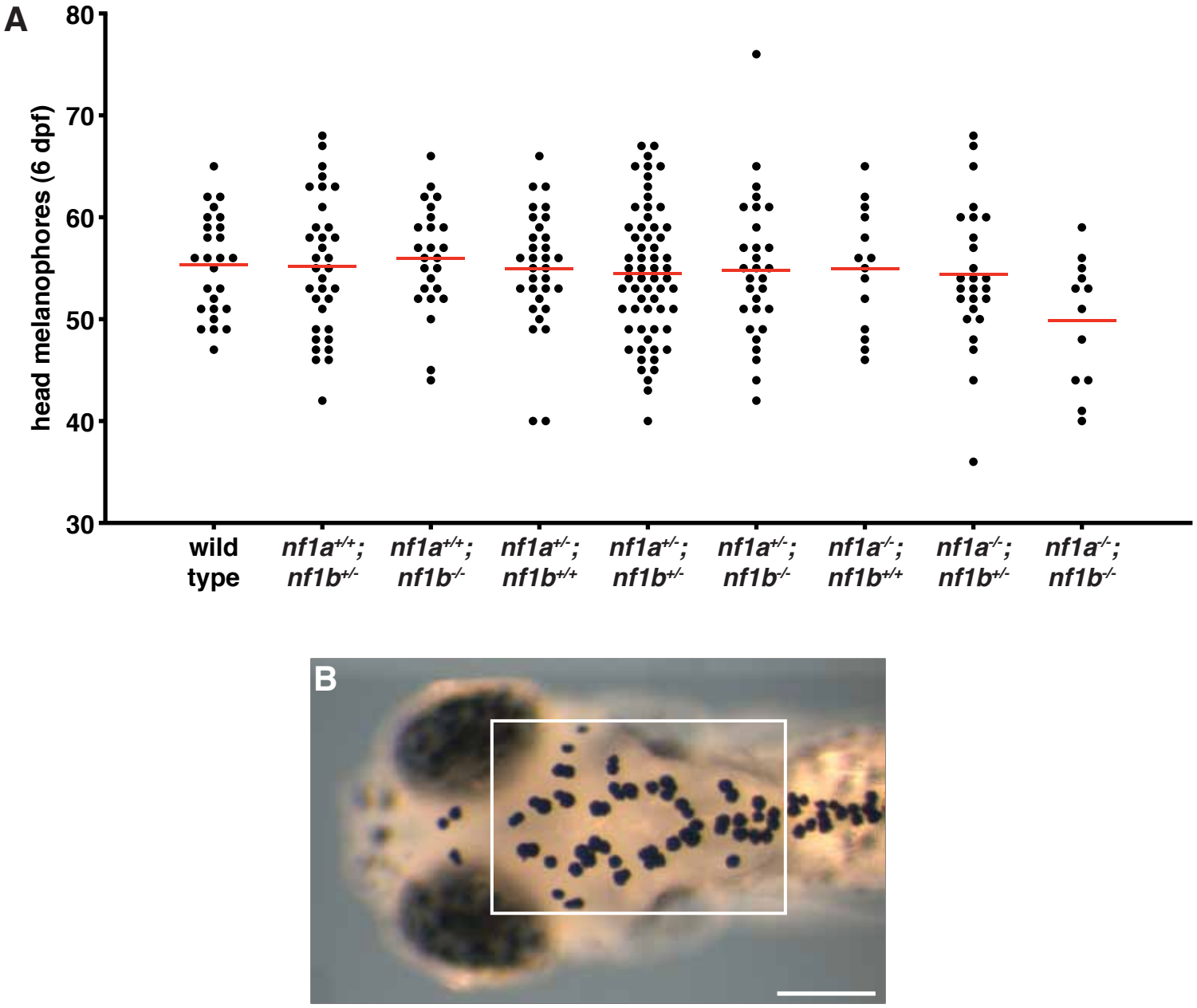

Fig. S14. Quantification of head melanophores in wild type and *nf1a*/*nf1b* mutant larvae at 6 dpf.
(A) Quantification of head melanophores from wild type (n=26), *nf1a*$^{+/+}$; *nf1b*$^{+/-}$ (n=34), *nf1a*$^{+/+}$; *nf1b*$^{-/-}$ (n=25), *nf1a*$^{+/-}$; *nf1b*$^{+/+}$ (n=32), *nf1a*$^{+/-}$; *nf1b*$^{+/-}$ (n=62), *nf1a*$^{+/-}$; *nf1b*$^{-/-}$ (n=30), *nf1a*$^{-/-}$; *nf1b*$^{+/+}$ (n=14), *nf1a*$^{-/-}$; *nf1b*$^{+/-}$ (n=26), and *nf1a*$^{-/-}$; *nf1b*$^{-/-}$ (n=12) larvae at 6 dpf. Each point represents the number of head melanophores in an individual embryo and red lines indicate mean values. (B) Representative image depicting head melanophores (boxed region) in a wild type larva at 6 dpf following epinephrine treatment and fixation. Scale bar: 200 μm.

Movie 1.

Movie 2.

Movie 3.